

# Hidden Monsters with SPHEREx

## I. A goldmine for heavily reddened quasars at cosmic noon

Matthew Stepney<sup>1,2,3,\*</sup>, Manda Banerji<sup>4</sup>, Franz E. Bauer<sup>2</sup>, Roberto J. Assef<sup>3</sup>, and Guodong Li<sup>5</sup>

<sup>1</sup> Centro de Astrofísica Y Tecnologías Afines, Av. Vicuña Mackenna 4860, San Joaquín, Santiago, Chile

<sup>2</sup> Instituto de Alta Investigación, Universidad de Tarapacá, Casilla 7D, Arica, Chile

<sup>3</sup> Instituto de Estudios Astrofísicos, Facultad de Ingeniería y Ciencias, Universidad Diego Portales, Av. Ejército Libertador 441, Santiago, Chile

<sup>4</sup> School of Physics and Astronomy, University of Southampton, Southampton, SO17 1BJ, UK

<sup>5</sup> Kavli Institute for Astronomy and Astrophysics, Peking University, Beijing 100871, People's Republic of China

Received May 5, 2026

### ABSTRACT

**Aims.** Heavily reddened quasars (HRQs) are luminous, dust-obscured broad-line quasars thought to trace a short-lived phase of intense black hole growth and feedback. Previous studies have been limited by small sample sizes, restricting robust statistical analyses of their properties. We expand the census of the most luminous HRQs to enable population-level studies, aiming to connect their SEDs to other luminous quasar populations and place them in context within an evolutionary sequence for massive galaxy and black hole formation.

**Methods.** We assemble multi-wavelength broad-band photometry for the brightest ( $K_{AB} < 18$  mag) HRQ candidates and select AGN candidates with red near infra-red colours of  $(J - K)_{AB} > 1.6$ . We employ SPHEREx spectrophotometry to confirm the HRQs and determine redshifts. Detailed SED fitting allows us to compare these HRQs to other luminous quasar populations, including a control sample of hyper-luminous, unobscured *unWISE*-Gaia (Quaia) quasars, as well as luminous Hot Dust-Obscured Galaxies (Hot DOGs).

**Results.** We confirm 76 new HRQs with redshifts  $1.5 < z_{sys} < 3.9$ , dust-corrected optical continuum luminosities of  $\log_{10}(\lambda L_{\lambda}(3000\text{\AA}))[\text{erg s}^{-1}] > 47.0$  and line-of-sight extinctions  $0.4 < E(B - V) < 1.6$  ( $A_V \sim 1 - 5$  mag). This more than doubles the number of confirmed HRQs at  $z_{sys} > 1.5$  including the first 7 HRQs ever identified at  $z > 3$ . A UV excess consistent with scattered quasar emission is detected in 76 per cent of SPHEREx HRQs. We conclusively demonstrate that HRQs are hot-dust poor compared to blue quasars of similar luminosity and redshift. We find that the  $6\mu\text{m}$  continuum luminosities of HRQs are systematically fainter at fixed 3000Å continuum luminosity relative to blue Quaia quasars, suggesting that HRQs are deficient in both hot and warm dust components. This combination of depleted torus-scale dust reservoirs and higher luminosities compared to Hot DOGs and blue quasars supports a scenario in which HRQs represent a blow-out phase, when strong feedback has begun to clear the central regions of obscuring material.

**Key words.** Galaxies: evolution, quasars: general, Galaxies: photometry

### 1. Introduction

Dust-obscured black hole accretion likely marks an important stage in the co-evolution of galaxies and their central supermassive black holes (SMBHs) (Sanders et al. 1988; Hopkins et al. 2005; Hopkins et al. 2008; Di Matteo et al. 2005). This reddened quasar phase is thought to be a direct result of major-mergers, which peak in frequency during cosmic noon (Bluck et al. 2009; Man et al. 2012) - a period defined by rapid black-hole growth and star formation. In this paradigm, gas inflows fuel powerful initially dust-obscured, active galactic nuclei (AGN) while simultaneously inducing a starburst (Granato et al. 2004; Di Matteo et al. 2005; Hopkins & Elvis 2009). The presence of this dust can make radiatively driven outflows more efficient (e.g. Costa et al. 2018; Ishibashi et al. 2017; Ishibashi & Fabian 2022), meaning dusty/obscured quasar populations likely trace periods of extreme quasar-driven feedback.

Evidence of dust-driven feedback in red quasar populations is observable across multiple wavelengths. Extreme outflows in both the broad- and narrow-line regions have been identi-

fied in Extremely Red Quasars (ERQs; Zakamska et al. 2016; Hamann et al. 2017; Perrotta et al. 2019; Gillette et al. 2024), Hot Dust-Obscured Galaxies (Hot DOGs; Eisenhardt et al. 2012; Wu et al. 2012; Jun et al. 2020; Finnerty et al. 2020; Vayner et al. 2025) and Heavily Reddened Quasars (HRQs; Temple et al. 2019; Stepney et al. 2024), with kinetic powers comparable to or exceeding those of unobscured systems at similar luminosities. At radio wavelengths, compact emission correlates with dust extinction and, together with steep spectral slopes, favours an origin in wind-driven shocks within a dusty obscuring medium (Fawcett et al. 2023, 2025). Furthermore, high accretion rates, often reaching or exceeding their Eddington limits (e.g. Li et al. 2024; Stepney et al. 2026), further suggest that red quasars are caught during a brief phase of rapid black hole growth producing strong AGN feedback.

Numerous studies have also been devoted to understanding the spectral energy distribution (SED) properties of red quasar populations. For example, blue photometric colours at rest-UV wavelengths, arising from an excess in the continuum emission relative to the dust-obscured AGN, has been detected in Hot DOGs (Assef et al. 2016, 2020) and HRQs (e.g. Wethers et al.

\* Corresponding author: mstepney@cata.cl

2018; Stepney et al. 2026). While the origin of the UV excess is unclear, the detection of broad emission lines and polarised light in some Hot DOGs (e.g. Assef et al. 2016, 2020, 2022, 2025; Li et al. 2024) suggests that scattered quasar emission may contribute significantly. In comparison, observations of the HRQ ULASJ2315+0143 with VLT X-Shooter reveal both broad emission lines and host galaxy signatures, indicating that the UV-optical continuum may also arise, at least in part, from active star-forming regions within the quasar host galaxy (Stepney et al. 2024). Furthermore, red quasars exhibit a wide diversity in dust properties. The SEDs of Hot DOGs seem to be dominated by hot and warm dust components (e.g. Wu et al. 2012; Tsai et al. 2015; Li et al. 2023), whereas the SEDs of HRQs are comparatively hot-dust poor (Stepney et al. 2026).

Concerted efforts have been made to link the multi-wavelength SED properties of red quasars to their outflow and accretion characteristics in the context of galaxy evolution (e.g. Temple et al. 2019; Calistro Rivera et al. 2021; Stepney et al. 2024; Stepney et al. 2026). However, the relatively modest sample sizes of the reddest and most heavily obscured quasars limit our ability to robustly establish relationships between the different populations. For example, traditional ultraviolet (UV) and optical selection techniques used to select quasars for wide-field spectroscopic follow up as part of e.g. the Sloan Digital Sky Survey (SDSS; York et al. 2000) and Dark Energy Spectroscopic Instrument (DESI; Alexander et al. 2023) generally do not detect quasars with line-of-sight dust-extinctions  $E(B - V) \geq 0.5$  (Richards et al. 2003; Fawcett et al. 2020). Hence, assembling large, spectroscopically confirmed samples of the reddest quasars has remained a significant challenge.

Spectroscopic confirmation of luminous HRQs has previously been conducted through single-object NIR spectroscopic follow-up of candidates selected from wide-field infrared surveys (Banerji et al. 2012, 2013, 2015; Temple et al. 2019). As the most luminous and massive galaxies are rare with low sky-densities (Cole et al. 2001; Benson et al. 2003; Huang et al. 2003; Somerville et al. 2008; Schaye et al. 2015), luminous HRQ candidates are distributed across the entire sky, making confirmation of statistical samples expensive due to large slew times between targets. Fortunately, in the new era of wide-field/all-sky near-infrared spectroscopic/spectrophotometric surveys - e.g. Euclid (Euclid Collaboration et al. 2025a,b,c) and the Spectro-Photometer for the History of the Universe, Epoch of Reionization, and Ices Explorer (SPHEREx; Doré et al. 2014) - it is now feasible to assemble large, spectroscopically confirmed samples of highly dust-obscured quasars.

In this paper, we exploit the all-sky coverage of SPHEREx to confirm a new sample of hyper-luminous HRQs via spectrophotometry, enabling a comprehensive multi-wavelength SED analysis of the largest HRQ population assembled to date. This study demonstrates the potential of SPHEREx to conduct population studies of obscured quasars and marks the beginning of an ongoing effort to characterise the luminous, obscured quasar population. The structure of the paper is as follows; in Section 2, we describe the assembly of the multi-wavelength data used to select HRQ candidates. Source confirmation and redshift estimation are presented in Section 3, followed by a description of the SED modelling in Section 4. In Section 5, we introduce the hyper-luminous blue quasar sample used for comparison to the HRQs. We then examine the general properties of the SPHEREx-confirmed HRQ sample in Section 6, including comparisons with other quasar populations at similar luminosities and redshifts. We summarise our conclusions in Section 7. Here we report vacuum wavelengths throughout and adopt a  $\Lambda$ CDM

cosmology with  $h_0 = 0.71$ ,  $\Omega_M = 0.27$  and  $\Omega_\Lambda = 0.73$  for calculating luminosities.

## 2. Heavily Reddened Quasars (HRQs)

### 2.1. Infrared Selection

The selection of the original HRQ population is based on observed optical, near- and mid-infrared photometric colours and is discussed at length in Banerji et al. (2012), Banerji et al. (2013), Banerji et al. (2015) and Temple et al. (2019) - and summarised in Stepney et al. (2026). The primary selection of the HRQs is based on their red, observed ( $J - K$ ) colours. As the objective of this paper is to build a more complete sample of HRQs at the highest quasar luminosities, we make a number of modifications to the original HRQ selection criteria.

Firstly, we modify the original  $K$ -band magnitude limit ( $K_{AB} < 20.3$ ) such that only the brightest ( $K_{AB} < 18$ ) sources are selected. Second, given that  $> 80$  per cent of the original HRQ sample host a statistically significant rest-UV excess with respect to their rest-optical emission (Stepney et al. 2026 - see also Wethers et al. 2018), we omit the  $i$ -band magnitude limit ( $i_{AB} > 20.5$ ) and  $(i - K)_{AB} > 2.5$  colour selection used in Banerji et al. (2012) to select the original HRQ sample. Finally, given also that the HRQ population is hot-dust poor when compared to luminous blue quasars of similar luminosity and redshift (e.g. Stepney et al. 2024; Stepney et al. 2026), we relax the mid-infrared colour selection to be bluer, and use the Assef et al. (2018) R90 *WISE* AGN catalogue; corresponding to a 90 per cent reliability limit of all Wide-field Infrared Sky Explorer (*WISE*) AGN. The result is a more complete sample of luminous HRQ candidates, whose revised selection criteria are as follows;

- $K_{AB} < 18$
- $(J - K)_{AB} > 1.6$
- $(W1 - W2)_{Vega} > 0.5$
- $kclass = -1$  (point-source morphology in the  $K/K_S$ -band)

To gain near-infrared coverage across the northern and southern skies, we match the R90 *WISE* AGN catalogue to the United Kingdom Infrared Deep Sky Survey's (UKIDSS) Large Area Survey (UKIDSS-LAS DR10; Lawrence et al. 2007), the United Kingdom Infrared Telescope's Hemisphere Survey (UHS DR2; Dye et al. 2018) and the Visible and Infrared Survey Telescope for Astronomy's (VISTA) Hemisphere Survey (VHS DR5; McMahon et al. 2013, 2021) using a matching radius of  $1''^1$ . Given that HRQs have compact morphologies in the rest-optical (by selection), we use  $2''$  diameter aperture magnitudes from UKIDSS-LAS, UHS and VHS for our study, and profile fitting magnitudes from *WISE*.

Applying the above selection criteria yields 413 HRQ candidates spanning  $\approx 20,000 \text{ deg}^2$ . Nine sources are already spectroscopically confirmed HRQs from Banerji et al. (2012, 2015) and are therefore removed. An additional source - ULASJ2148-0011 - was previously identified in Banerji et al. (2012), but not spectroscopically confirmed via Gemini or VLT-SINFONI, therefore, this source remains in our candidate list. The total number of luminous HRQ candidates is therefore 404.

<sup>1</sup> Cone searches are conducted with v4.10-5 of the Tool for Operations on Catalogues And Tables (TOPCAT; Taylor 2005) software.

## 2.2. Multi-wavelength photometric data

A primary objective of this work is to build the full multi-wavelength spectral energy distributions (SEDs) of the new HRQ sample. Hence, we assemble a catalogue of optical photometry, probing the rest-frame UV SEDs, to complement our near- and mid-infrared data. We match all 404 luminous HRQ candidates to the second data release of the DECam Local Volume Exploration Survey (DELVE-DR2; Drlica-Wagner et al. 2022)<sup>2</sup> with a 1'' search radius via the NOIRLab Astro Data Lab Service (Fitzpatrick et al. 2014; Nikutta et al. 2020; Juneau et al. 2021) - resulting in 332 matches. To extend our coverage at northern latitudes, we also match the sample to the Sloan Digital Sky Survey (SDSS-DR16; Ahumada et al. 2020). This yields 215 matches, resulting in rest-UV/optical coverage for 389 HRQ candidates via DELVE, SDSS, UKIDSS-LAS, UHS, VHS and *WISE*. Given that many HRQs have extended morphologies in the rest-frame UV (e.g. Wethers et al. 2018; Stepney et al. 2024), we use MAG\_AUTO photometric extractions for both DELVE and SDSS. Since UKIDSS-LAS, UHS and VHS avoid the galactic plane, we do not perform a Milky Way galactic-extinction correction to the optical bands. While this may introduce an additional source of uncertainty to the SED fitting, the error budget will still be dominated by uncertainties in the photometric extraction (particularly in fainter sources) as well as the relative simplicity of our SED model.

## 3. Spectrophotometric confirmation with SPHEREx

### 3.1. SPHEREx data acquisition

SPHEREx is a National Aeronautics and Space Administration (NASA) Explorer satellite poised to complete the first all-sky spectral survey at near-infrared wavelengths (Doré et al. 2014; Bock et al. 2026). SPHEREx observes in 102 dedicated spectral channels whose wavelength coverage spans  $0.75 - 5.0\mu\text{m}$ , with estimated  $5\sigma$  depths of  $\sim 19.5 - 19.9$  AB magnitudes at  $0.75 < \lambda < 3.2\mu\text{m}$  by the time of the survey's completion, and a 6'' pixel scale (Doré et al. 2014; Bock et al. 2026). While SPHEREx has already been utilised for cosmological and interstellar ice studies (e.g. Xia et al. 2025; Boersma et al. 2026; Lisse et al. 2026), this work represents one of the first studies in which SPHEREx has been used to identify dust-obscured broad-line quasars, although the suitability of SPHEREx for this application was first highlighted by Kim et al. (2024). Recently Davies et al. (2026) have also used SPHEREx to confirm 87 new luminous quasars at  $4.0 < z_{\text{sys}} < 5.7$  as well as lower-redshift interlopers.

To acquire SPHEREx spectra for our 404 HRQ candidates, we use the Infrared Science Archive's (IRSA's) Spectrophotometry Tool<sup>3</sup>, which implements a multi-stage data processing pipeline to perform photometric extractions, photometric/wavelength calibrations, and background subtractions of the SPHEREx data in real time (Akeson et al. 2025). In all cases, we used a 15 pixel aperture for background estimation and a point-source morphology for the forced photometric extraction<sup>4</sup>.

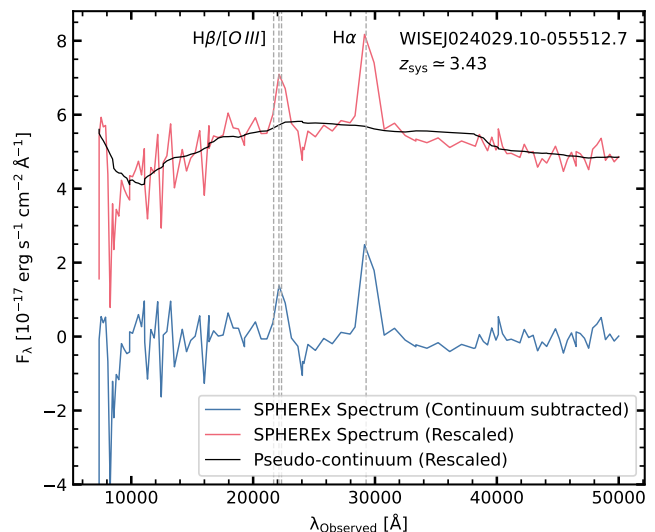


Fig. 1: The continuum-subtracted SPHEREx spectrum of the confirmed HRQ - WISEJ024029.10-055512.7 - is presented in blue. To aid readability the original SPHEREx spectrum (red) and corresponding 29-pixel median-filtered pseudo-continuum (black) have been shifted +4 units in the y-direction. The positions of the broad Balmer emission lines are marked in grey.

### 3.2. Estimating quasar redshifts with SPHEREx

While the SPHEREx Science Team will eventually build high-level SPHEREx data products which include redshift estimates (e.g. level 4 processing; Akeson et al. 2025), they are not publicly available at present. Hence, we employ a cross-correlation approach similar to Hewett & Wild (2010) - and subsequently Rankine et al. (2020) and Stepney et al. (2023) - to determine the redshifts of the HRQ candidates. Our approach consists of two steps; (i) the definition of a smooth pseudo-continuum from which continuum-subtracted SPHEREx spectra can be defined and (ii) a cross correlation algorithm that uses a resampled quasar template spectrum to estimate the redshift of each source.

#### 3.2.1. Defining the pseudo-continuum

Given that the shape of the quasar continuum can vary depending on the SED of the quasar, we define the pseudo-continuum empirically following Hewett & Wild (2010). Specifically, the quasar pseudo-continuum is defined by a median-filtered version of the original SPHEREx spectrum, which is reflected at the blue and red ends and stitched together to negate edge effects. We find that the ideal filtering window for the SPHEREx spectra is 29 channels, beyond which there is no significant improvement to the pseudo-continuum. An illustration of how our continuum subtraction recipe operates in practice is presented in Fig. 1.

#### 3.2.2. Cross-correlation analysis

Our cross-correlation analysis scheme is similar to that described in section 4.2 of Hewett & Wild (2010) with two key differences. First, the template used for the cross-correlation scheme is generated by *QSOGEN*<sup>5</sup>, a Python package that implements

result in a lower spectral resolution than reported in some objects, and consequently, increased uncertainties in our redshift estimates.

<sup>5</sup> <https://github.com/MJTemple/qsozen>

<sup>2</sup> <https://delve-survey.github.io>

<sup>3</sup> <https://irsa.ipac.caltech.edu/applications/spherex/tool-spectrophotometry>

<sup>4</sup> The SPHEREx spectra used in this work were downloaded between January and February 2026, however, the SPHEREx data is still accumulating as of the publication date of this manuscript. Therefore, some objects may not have been observed in all spectral channels. This could

an empirically-motivated parametric model to simulate quasar colours, magnitudes and SEDs (Temple et al. 2021b). To produce the template spectrum, we generate a QSOGEN quasar model (with all free parameters left at their default), which reproduces the spectrum of the average SDSS quasar. The reddening primarily affects the shape of the quasar continuum, which is subtracted before the cross-correlation is conducted. We resample this template spectrum onto the SPHEREx spectral resolution, and subtract the continuum in the same manner as detailed in Section 3.2.1. The cross-correlation between each template and an individual HRQ spectrum is performed with the HRQ redshift as a free parameter, with bad SPHEREx pixels masked beforehand. Hence, cross-correlation coefficients are calculated across redshift-space, with the redshift solutions varying in 0.01 increments - i.e.  $\Delta z_{\text{sys}} = 0.01$ .

To estimate redshift uncertainties, each SPHEREx spectrum is perturbed by Gaussian noise consistent with the corresponding noise array, and the mean and standard deviation after 100 iterations are used to determine our final results. To ensure that our uncertainty estimates are robust, we performed a cross-correlation analysis on the SPHEREx spectra of nine already confirmed HRQs. We find that the average difference in redshift between the SPHEREx estimates and those from higher-resolution ground-based spectroscopy is  $\langle \Delta z_{\text{sys}} \rangle \approx 0.011$ , broadly consistent with the average Monte-Carlo uncertainties calculated for the remaining sample - e.g.  $\langle \Delta z_{\text{sys}} \rangle \approx 0.006$ . As the uncertainties associated with the SPHEREx spectral channels are likely underestimated (e.g. Davies et al. 2026), the slightly underestimated Monte-Carlo errors are expected.

The redshift solution that maximises the cross-correlation coefficient for a given SPHEREx spectrum is assigned as the systemic redshift provided that: (i) the cross-correlation coefficient meets the threshold,  $cc(z_{\text{sys}}) \geq 0.5$  and (ii) the redshift solution meets the threshold,  $z_{\text{sys}} \geq 1.5$ . The former condition is determined empirically and is more conservative than the  $cc(z_{\text{sys}}) \geq 0.2$  used in Hewett & Wild (2010) who relied on the SDSS spectroscopic pipeline already minimizing catastrophic redshift misidentifications. The  $z > 1.5$  cut is imposed because the HRQ selection results in impure quasar samples at low redshift ( $z_{\text{sys}} \leq 0.6$ ) with many low redshift HRQ candidates being morphologically compact star-forming galaxies (e.g. SDSSJ210050.13-005752.5; Banerji et al. 2015). Additionally, at  $0.6 \leq z_{\text{sys}} \leq 1.5$ , contributions from the host galaxy at  $\sim 1\mu\text{m}$  can bias the SED fitting at near-infrared wavelengths (e.g. Stepney et al. 2026). Hereafter, when referring to HRQs we consider only the cosmic noon sub-sample from Stepney et al. (2026) and this work.

There are 305 SPHEREx objects for which our cross-correlation analysis yields coefficients that are too low to meet criterion (i), and a further 20 objects whose optimum redshift is too low to meet criterion (ii). Hence, the result is 76 SPHEREx-confirmed HRQs with redshifts  $1.5 < z_{\text{sys}} < 3.9$  including, for the first time, 7 HRQs with  $z_{\text{sys}} > 3.0$ . Figure 2 shows typical example spectra for SPHEREx objects that fail either criterion (i) or (ii), in addition to an object that satisfies both. Objects that fail criterion (i) generally have spectra that is either noise-dominated or featureless. The featureless sources may be morphologically compact galaxies or narrow-line AGN, whose nebular emission lines are too narrow and/or weak to be detected at the resolution of SPHEREx - resulting in poor redshift estimates. Objects that fail only criterion (ii) have significant  $H\alpha$  emission ( $S/N > 3$ ) and have robust redshifts, however, they trace a separate population to the cosmic noon HRQs due to selection effects (Stepney et al. 2026).

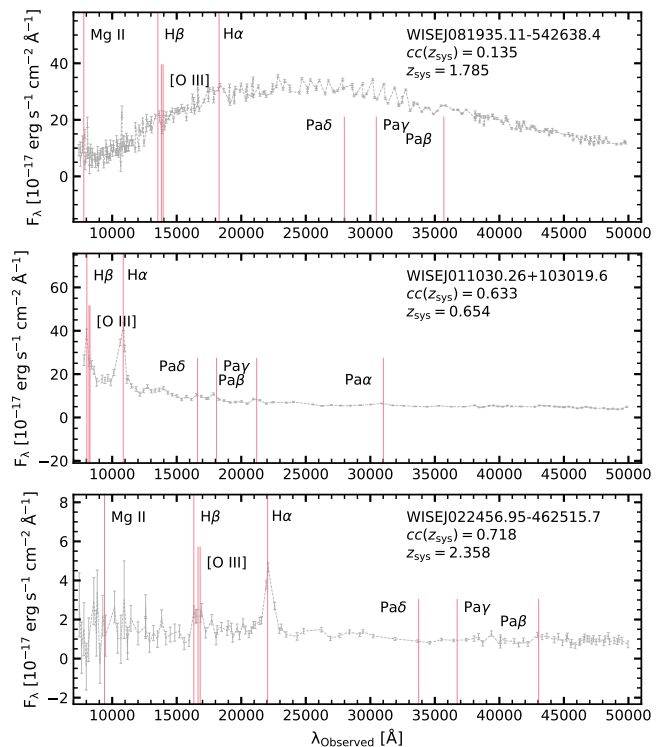


Fig. 2: We present example continuum-subtracted SPHEREx spectra for sources that; fail to meet the  $cc(z_{\text{sys}}) \geq 0.5$  threshold (top), fails to meet the  $z_{\text{sys}} \geq 1.5$  threshold (middle) and meet both criteria (bottom). The best redshifts and cross-correlation coefficients are shown in the upper right. In the middle/bottom panels the broad  $H\alpha$  emission line is clearly visible. In the top panel, the SPHEREx spectrum is featureless, and hence the cross-correlation analysis cannot robustly determine a redshift.

Given the low spectral resolution in the bluer spectral channels of SPHEREx ( $R \approx 40$  at  $0.75 - 3.8\mu\text{m}$ ; Doré et al. 2014), robust  $H\alpha$ -derived black hole mass measurements are unfeasible at the redshifts probed by this study and are therefore not attempted, however, when fit with a single Gaussian the full-width at half-maximum of the  $H\alpha$  line profiles range between  $6000 - 8000 \text{ km s}^{-1}$ . Our final HRQ sample, with some example SPHEREx spectra, is presented in Appendix A.

#### 4. HRQ spectral energy distribution modelling

In this section, we describe the spectral energy distribution (SED) model used to fit the full suite of multi-wavelength data assembled in Section 2.1 for the SPHEREx HRQ sample.

##### 4.1. The multi-wavelength SED properties of HRQs from broad-band photometry

We model the SEDs with QSOGEN (see Section 3.2 and the references within) and adopt a Monte-Carlo approach for the fitting, making use of the EMCEE<sup>6</sup> Python package to explore the likelihood space via the affine-invariant ensemble sampler proposed by Goodman & Weare (2010). Given that many HRQs (>80 per cent) host blue photometric colours at rest-UV wavelengths (e.g.

<sup>6</sup> <https://github.com/dfm/emcee>

Wethers et al. 2018; Stepney et al. 2024; Stepney et al. 2026), we adopt the same two-component model used in Stepney et al. (2024) and Stepney et al. (2026).

The SED model comprises a dust-attenuated quasar component and an additional scattered light component, which we use to reproduce the rest-UV photometry. While this approach is well-motivated (e.g. broad high-ionisation emission lines are detected at rest-UV wavelengths in a VLT-XShooter spectrum of the HRQ - ULASJ2315+0143; Stepney et al. 2024), the shape of the rest-UV continuum in HRQs remains consistent with both scattered quasar light and on-going star formation in the quasar host (Wethers et al. 2018; Stepney et al. 2024); therefore, a host galaxy contribution at rest-UV wavelengths cannot be ruled out, indeed, Stepney et al. (2024) argue that both host galaxy emission and scattered quasar light are likely to contribute to the rest-UV emission of HRQs (see also - Section 6.3). Given the degeneracy between the two interpretations of the UV excess, we adopt only the scattered light interpretation for the purposes of fitting the broad-band photometry of HRQs because the model contains fewer free parameters.

At redder wavelengths, the host galaxy can have a measurable contribution to the total SED in luminous blue quasars. For example, in SDSS quasars, the inclusion of the S0 template from the SWIRE library (Polletta et al. 2007) improved the  $Q_{SOGEN}$  SED fit at  $\lambda_{rest} \sim 1\mu m$ , with an average contribution to the total SED of 5-10 per cent (section 2.5; Temple et al. 2021b). However, the relative contribution of the host galaxy decreases with increasing quasar luminosity (e.g. Richards et al. 2006; Vanden Berk et al. 2006), with SDSS samples following the relation  $L_{galaxy} \propto L_{QSO}^{0.684}$  (section 5; Temple et al. 2021b). Given that the average HRQ is  $\sim 2.5$  dex brighter than the average SDSS quasar, this corresponds to a relative host galaxy contribution of  $< 1$  per cent when extrapolated to HRQ luminosities. Hence, in Stepney et al. (2026), the inclusion of the S0 host-galaxy template only produced favourable SED fits in lower redshift sources whose luminosities  $\log_{10}(\lambda L_{\lambda}(3000\text{\AA}))[\text{erg s}^{-1}] < 46$ . Additionally, when fitting a star-forming host galaxy component to the VLT-XShooter spectrum of the HRQ, ULASJ2315+0143, the host galaxy contribution was  $< 1$  per cent in the  $H\alpha$  emission region (Stepney et al. 2024). As the rest-optical to NIR emission of HRQs has been shown to be completely dominated by the quasar in previous works, we do not account for contributions from the host galaxy when modelling their SEDs.

Therefore, the free parameters used to model our HRQ SEDs are as follows: (i) the dust-corrected  $3000\text{\AA}$  continuum luminosity of the quasar,  $\log_{10}(\lambda L_{\lambda}(3000\text{\AA}))[\text{erg s}^{-1}]$ ; (ii) the line-of-sight dust extinction,  $E(B - V)$ , (iii) the ratio in luminosity between the hot-dust blackbody and the tail of the quasar UV/optical continuum slope at  $2\mu m$ ,  $L_{Dust}/L_{Disk|2\mu m}$ , which can be used as a proxy for the amplitude of the hot dust emission (e.g. Figure 1; Temple et al. 2021a); and (iv) the scattering fraction,  $F_{UV}$ , which represents a fixed fraction of the total unobscured quasar emission. Since the average UV inflection wavelength of the HRQ SED is  $\sim 2500\text{\AA}$  (Stepney et al. 2026), we only fit the two-component SED model to objects with observed-optical broad-band photometry. Objects with no rest-UV photometric data are fit with the dust-reddened quasar component only.

In our SED model, the hot-dust blackbody component is described by a single free parameter. Its effective temperature is fixed at  $T_{bb} \simeq 1243\text{ K}$ , corresponding to the mean blackbody temperature derived from SED fits to blue SDSS quasars and consistent with the sublimation temperature of sili-

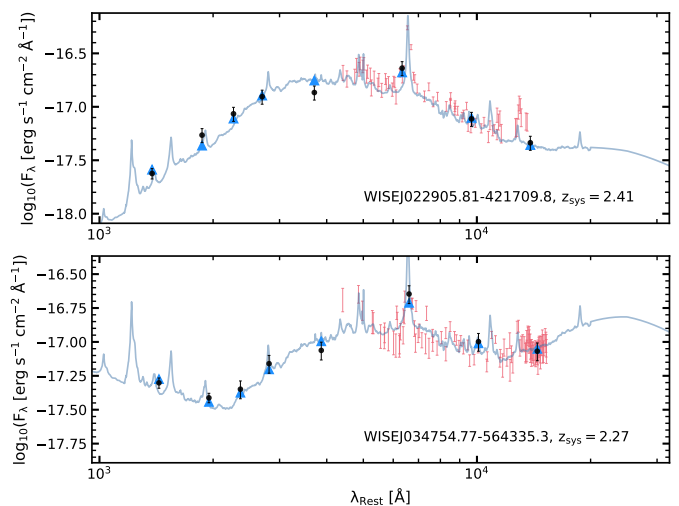


Fig. 3: The "best-fit"  $Q_{SOGEN}$  SEDs for two SPHEREx-confirmed HRQs, one where the inclusion of a scattered component was rejected (top) and one where the scattered component was confirmed (bottom). The broad-band photometric data from DELVE, UKIDSS/VHS and WISE are indicated in black with their associated uncertainties. The best-fit SED models are shown as blue lines and triangles while the SPHEREx spectra are overlaid in red.

cate dust (Rosa et al. 2013; Temple et al. 2021a). Consequently, the only parameter that must be constrained is the hot-dust ratio,  $L_{Dust}/L_{Disk|2\mu m}$ . For quasars at  $1.5 < z_{sys} < 2.7$ , the W2 ( $4.6\mu m$ ) filter provides sufficient sensitivity to constrain this ratio to within  $\Delta L_{Dust}/L_{Disk|2\mu m} = 0.25$ , assuming the average W2 uncertainty of 0.028 mag. Similarly, at  $3.2 < z_{sys} < 4.0$ , the W3 ( $12\mu m$ ) filter constrains the hot-dust ratio to the same precision, assuming the average W3 uncertainty of 0.054 mag. However, for the seven HRQs with  $2.7 < z_{sys} < 3.2$ , the hot-dust ratio may be poorly constrained, since the W2 filter no longer robustly probes the hot-dust emission while the W3 filter samples rest-frame wavelengths redward of  $3\mu m$ .

A total of 68 objects have sufficient wavelength coverage to robustly test for a UV excess. We impose the following criteria for the UV excess to be considered statistically significant: (i) the scattered component must contribute at least 50 per cent of the flux to the blue-most photometric band and (ii) the two-component SED model must represent an improvement over the single-component dust-reddened quasar SED at  $> 99$  per cent confidence, i.e.  $\Delta\chi^2 > 6.63$  (See Table 1; Avni 1976). An example of an HRQ whose UV excess has been rejected/confirmed is presented in Fig. 3.

#### 4.2. Leveraging SPHEREx spectra for better constraints in the near-infrared

The spectral coverage at rest-frame near-infrared wavelengths is limited when relying solely on broad-band WISE photometry. The inclusion of SPHEREx spectra enables significantly stronger constraints on the hot-dust properties of HRQs. Given the  $6''$  spatial resolution of SPHEREx (Doré et al. 2014), we restrict our analysis to sources whose nearest  $K$ -band neighbour lies at an angular separation greater than  $6''$ , thereby minimizing contamination. Hence, we are able to conduct additional SED fitting including SPHEREx spectra for 70/76 HRQs, which is con-

sistent with the  $\sim 10$  per cent contamination rate from interlopers reported in Davies et al. (2026).

For the fitting, we adopt Gaussian priors informed by the results of Section 4.1 and fit the dust-reddened quasar + scattered-light SED model to the SPHEREx spectra of each source. Only spectral channels with signal-to-noise ratios  $S/N > 5$  are included in the fitting procedure. Owing to degeneracies among the free parameters (see Stepney et al. 2024, for a full discussion), we perform a final round of SED fitting using the broad-band photometry alone, imposing strict Gaussian priors on the hot-dust amplitude. This final fitting step accounts for any variations in the inferred luminosity, line-of-sight dust extinction, and scattering fraction induced by adjustments to the hot-dust component, particularly for sources where the SPHEREx spectral coverage does not extend sufficiently blueward to constrain the rest-frame UV emission. On average, this approach improves constraints on the hot-dust amplitude by a factor of seven.

A final summary of our SED analysis, in addition to example SED fits, are presented in Appendix B. Table B.1 will also be made available as online supplementary material. We find that the median reduced chi squared statistic for the HRQ SED fitting is  $\overline{\chi^2}_{\nu}|_{\text{Med}} = 1.6$ , broadly consistent with the performance of our SED model on the original HRQ sample (e.g.  $\overline{\chi^2}_{\nu}|_{\text{Med}} = 1.9$ ; Stepney et al. 2026).

## 5. A luminous control sample of blue quasars

As shown in Stepney et al. (Figure 1; 2026), many objects in the original HRQ sample already exhibit substantially higher rest-frame optical continuum luminosities after correcting for dust, compared to blue SDSS quasars which have been fit using the same SED models (e.g. Temple et al. 2021a, Temple et al. 2023 and Stepney et al. 2023). This is because SDSS samples are incomplete at the highest quasar luminosities ( $\log_{10}\{\lambda L_{\lambda}(3000\text{\AA})[\text{erg s}^{-1}]\} \gtrsim 46.5$ ) due to an  $i_{\text{AB}} > 15$  magnitude limit, which was imposed to prevent saturation and crosstalk in the spectrograph (Richards et al. 2006; Schneider et al. 2010). Since the selection presented in Section 2.1 features a brighter  $K_{\text{AB}}$ -band magnitude limit than previous work (e.g. Banerji et al. 2012, 2013, 2015; Temple et al. 2019), it is likely that our study will probe only the brightest HRQs. Consequently, we must construct a new control sample of blue quasars with luminosities comparable to the high-luminosity end of the HRQ distribution.

We begin with the bright ( $G_{\text{AB}} < 20$  mag) Gaia-*unWISE* Quasar Catalog (Quaia; Storey-Fisher et al. 2024) - which contains  $\sim 750,000$  quasar candidates with Gaia  $G$ ,  $BP$ , and  $RP$  measurements, *unWISE*  $W1$  and  $W2$  observations, and Gaia-estimated quasar classifier (QSOC) redshifts<sup>7</sup>. To determine a magnitude limit that ensures our blue quasar control sample has luminosities consistent with the HRQ sample, we use QSOGEN to simulate 10,000 blue quasar SEDs whose free-parameters are defined as follows;  $\log_{10}\{\lambda L_{\lambda}(3000\text{\AA})[\text{erg s}^{-1}]\} = 46.5 - 47.5$ <sup>8</sup>,  $E(B - V) = -0.1 - 0.2$ <sup>9</sup> and  $1.5 \leq z_{\text{sys}} \leq 4.0$ . Next, we compute the Gaia  $G$ -band magnitudes for each simulated SED and adopt a  $G_{\text{AB}} < 18$  magnitude limit to ensure sufficiently bright

sources, yielding an initial sample of 30,170 objects - 9,112 of which have redshifts  $1.5 \leq z_{\text{sys}} \leq 4.0$ .

To enable a full multi-wavelength SED analysis of the cosmic noon Quaia control sample, we cross-match the  $G_{\text{AB}} < 18$  Quaia sample with DELVE-DR2 (Drlica-Wagner et al. 2022), SDSS-DR16 (Ahumada et al. 2020), UKIDSS-LAS (Lawrence et al. 2007), UHS (Dye et al. 2018), and VHS (McMahon et al. 2013), following the procedure outlined in Section 2.1. This yields 5,329 sources that have coverage in the optical (either from DELVE or SDSS) and NIR (from either VHS, UHS or UKIDSS-LAS). We then match to R90 (e.g. Assef et al. 2018) to gain  $W3$  coverage and ensure that the rest-NIR SED is constrained across all redshifts. This final sample contains 4,711 sources, 1,618 of which are in SDSS DR16Q and 3 of which overlap with the *WISE*-SDSS selected hyper-luminous quasar sample (WISSH; Weedman et al. 2012). When fitting the broad-band photometry via QSOGEN we use the following free parameters;  $\log_{10}\{\lambda L_{\lambda}(3000\text{\AA})[\text{erg s}^{-1}]\}$ ,  $E(B - V)$  and  $L_{\text{Dust}}/L_{\text{Disk}}|_{2\mu\text{m}}$ . The median reduced chi squared statistic for the Quaia SED fits is  $\overline{\chi^2}_{\nu}|_{\text{Med}} = 1.4$ .

The accuracy of the Gaia-estimated QSOC redshifts increases with flux, i.e.  $|\Delta z_{\text{sys}}| < 0.1$  for 80 per cent of quasars with  $G_{\text{AB}} < 18.5$  (Storey-Fisher et al. 2024). To better understand the quality of the Quaia QSOC redshifts in our blue control sample, we obtain SPHEREx spectrophotometry for the 500 most luminous Quaia quasars (i.e. the regime in which SDSS was not used to verify the Gaia QSOC redshifts) and perform a cross-correlation analysis, following the same procedure outlined in Section 3. The average discrepancy between redshift estimates is  $\langle \Delta z_{\text{sys}} \rangle = 0.08$ , with  $|\Delta z_{\text{sys}}| < 0.2$ , or equivalently  $|\Delta z_{\text{sys}}/(1 + z_{\text{sys}})| \lesssim 0.1$ , for 95 per cent of the sample. Hence, for the purposes of broad-band SED fitting we assume that the Gaia-estimated QSOC redshifts are reliable. The result of SED-fitting to the bright Quaia control sample, are consistently measured quasar luminosities and hot-dust amplitudes for the HRQs and the blue quasars.

## 6. Connecting the different populations of luminous quasars at cosmic noon

In this section, we place our SED fitting results in the broader context, taking advantage of the substantially expanded sample constructed via our SPHEREx analysis. We compare the HRQ population to the luminous blue Quaia sample (Section 5) as well as Hot Dust-Obscured Galaxies (e.g. Hot DOGs; Eisenhardt et al. 2012; Assef et al. 2015, 2020) - another class of very luminous obscured AGN, but with typically higher continuum extinctions than the HRQs.

### 6.1. A unified sample of hyper-luminous HRQs

Figure 4 illustrates the redshift and dust-corrected 3000Å quasar continuum luminosity distributions for both the original and SPHEREx HRQ populations. The SPHEREx HRQs are generally consistent with the original HRQ samples, however, they tend towards higher luminosities and extend to higher redshifts. The luminosity bias between the two HRQ samples owes to the brighter  $K$ -band magnitude selection imposed on the SPHEREx HRQ sample (see Section 2.1). The larger redshifts stem from the broader and more complete wavelength coverage of SPHEREx (e.g.  $0.75 - 5.0\mu\text{m}$ ; Doré et al. 2014; Bock et al. 2026) compared to VLT-SINFONI (e.g.  $1.10 - 2.45\mu\text{m}$ ; Eisenhauer et al. 2003) and Gemini-GNIRS, which are

<sup>7</sup> The QSOC module estimates redshifts by using a chi-squared approach to compare BP/RP spectra for each quasar candidate to an SDSS composite spectrum, a more detailed discussion is presented in Storey-Fisher et al. (2024) and the references within

<sup>8</sup> Consistent with the original HRQ sample Stepney et al. (2026).

<sup>9</sup> Consistent with the range in line-of-sight dust-extinction observed amongst blue SDSS quasars (Temple et al. 2021a).

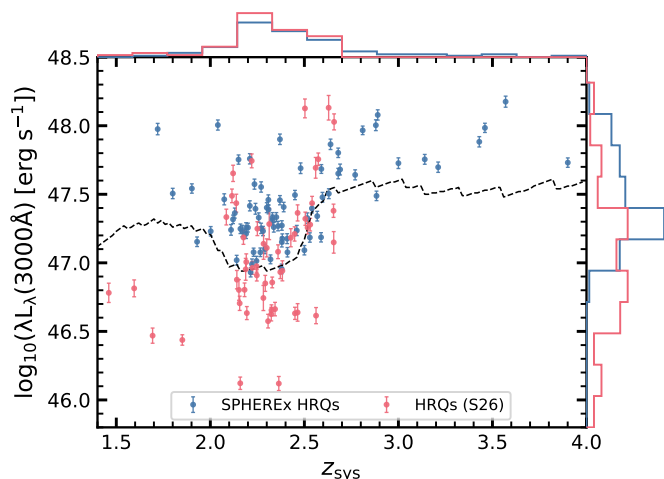


Fig. 4: The dust-corrected 3000Å continuum luminosity of the quasar vs redshift. The marginalised distributions are presented as histograms on their corresponding axis. SPHEREx HRQs are shown in blue and the original  $z_{\text{sys}} \geq 1.5$  HRQ sample (Stepney et al. 2026) is shown in red. The SPHEREx HRQs are biased to higher luminosities (due to our brighter  $K$ -band selection) and extend to higher redshifts. The black dashed line represents the minimum luminosity required for a quasar to meet the  $K_{\text{AB}} < 18$  magnitude limit at the minimum dust-extinction that satisfies the  $(J - K)_{\text{AB}} > 1.6$  colour selection.

both ground-based and are therefore affected by atmospheric band gaps (Elias et al. 2006).

In Fig. 4, we also see that lower 3000Å continuum luminosities are required to satisfy our HRQ selection at  $2.0 \lesssim z_{\text{sys}} \lesssim 2.5$ . This is due to the presence of the broad  $H\alpha$  emission in the  $K$ -band at these redshifts, which has the effect of boosting the  $K$ -band flux. This results in a significantly larger number of HRQs with redshifts of  $2.0 \lesssim z_{\text{sys}} \lesssim 2.5$  in both the SPHEREx and original samples (e.g. Banerji et al. 2012, 2013, 2015; Temple et al. 2019). In addition, the newly confirmed SPHEREx HRQs have line-of-sight dust extinctions,  $E(B - V)$ , consistent with the original HRQs, with a median  $E(B - V)|_{\text{Med}} = 0.8$  in both  $z_{\text{sys}} \geq 1.5$  samples (Stepney et al. 2026). Taken together, we conclude that the SPHEREx sample is consistent with previous work and therefore comprises true HRQs. Henceforth, we treat the SPHEREx and original HRQ samples as a single unified population comprised of 127 objects at  $z_{\text{sys}} \geq 1.5$ .

In Fig. 5, we find that HRQs extend to higher luminosities than the Quiaia control sample, although there is significant overlap at more modest HRQ luminosities. While we expect that the SPHEREx HRQs probe the most extreme end of the HRQ luminosity distribution, there is a clear deficit of blue Quiaia counterparts at  $\log_{10}\{\lambda L_{\lambda}(3000\text{\AA})[\text{erg s}^{-1}]\} > 47.5$ . This suggests that the number densities of red quasars may exceed that of their blue counterparts in the highest luminosity regime. This result is consistent with Banerji et al. (2015), although a more comprehensive investigation is deferred to future work; where we will push to fainter, more complete and much larger statistical samples with SPHEREx (e.g. Stepney et al., in prep.). In addition to blue quasars, the optical luminosities of our brightest HRQs ap-

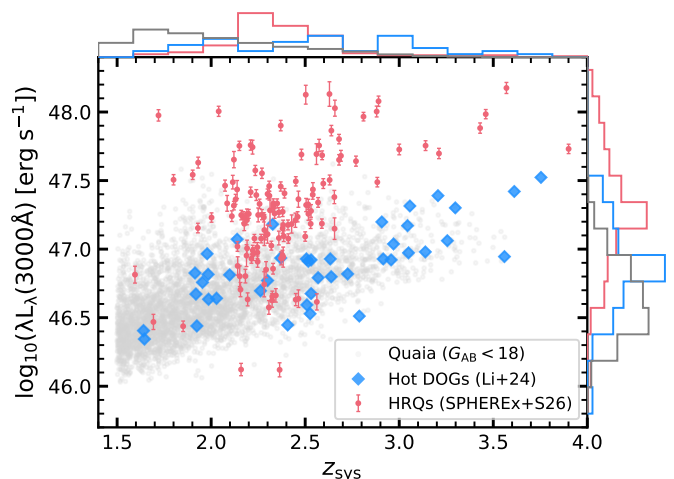


Fig. 5: The dust-corrected 3000Å continuum luminosity vs redshift. The combined HRQ sample from this paper and Stepney et al. (2026) is shown in red and our Quiaia  $G_{\text{AB}} < 18$  mag control quasars (e.g. Storey-Fisher et al. 2024) are shown in grey. Blue Hot DOGs (e.g. Li et al. 2024) are represented by blue diamonds. HRQs tend towards higher luminosities than both blue quasars and Blue Hot DOGs.

pear to exceed that of the Hot DOG population<sup>10</sup>. While this result may, at least in part, be as a result of differences between the SED modelling methodologies, it is consistent with reports that HRQs generally have higher accretion rates than their Hot DOG counterparts (e.g. Li et al. 2024; Stepney et al. 2026) and may suggest that Hot DOGs represent an earlier stage in the black hole feeding process.

## 6.2. Depleted hot-dust reservoirs as evidence for feedback

A key result from Stepney et al. (2026) is that HRQs represent a phase of black hole accretion characterised by a substantial depletion of the hot-dust reservoir. In this section, we test whether this result persists with our now significantly larger sample of HRQs. In Section 2.1, we re-defined the HRQ selection by relaxing the mid-infrared colour threshold to  $(W1 - W2)_{\text{Vega}} > 0.5$ . In Appendix C, we confirm that the modification to our selection criteria now enables a complete study of HRQ hot-dust properties. We measure an average hot-dust amplitude of  $\langle L_{\text{Dust}}/L_{\text{Disk}}|_{2\mu\text{m}} \rangle_{\text{HRQ}} = 1.3 \pm 0.9$  for all HRQs - significantly lower than the Quiaia average of  $\langle L_{\text{Dust}}/L_{\text{Disk}}|_{2\mu\text{m}} \rangle_{\text{Quiaia}} = 4.3 \pm 1.3$ . Furthermore, by using the definition for 'hot-dust poorness' invoked by Jiang et al. (2010) and Jun & Im (2013) in their respective studies of blue quasars, we find that 21/127 HRQs (17 per cent) are formally "hot-dust poor". This represents a significantly higher fraction than the blue Quiaia sample, with just 15/4711 (0.3 per cent) of blue quasars meeting the Jiang et al. (2010) condition. Hence, with a larger and more complete sample of HRQs, our results are consistent with the conclusions presented in Stepney et al. (2026).

Figure 6 (left) shows how the hot-dust amplitudes (when possible to constrain) of both blue Quiaia quasars (Section 5) and HRQs vary as a function of  $6\mu\text{m}$  continuum luminosity, which

<sup>10</sup> To calculate the 3000Å continuum luminosities of the Hot DOG sample, we apply the Netzer (2019) luminosity-dependent corrections to the 5100Å continuum luminosities calculated in Li et al. (2024).

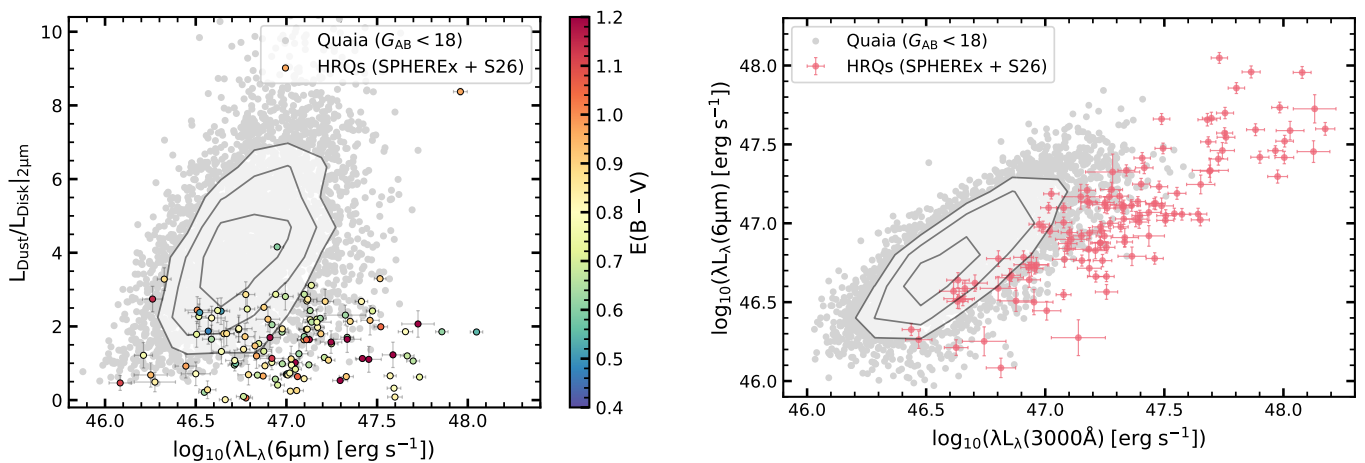


Fig. 6: The  $2\mu\text{m}$  hot-dust emission amplitude as a function of  $6\mu\text{m}$  continuum luminosity (left) for luminous Quiaia quasars (grey) and HRQs (coloured circles). Density contours encircle 25, 50 and 68 per cent of the Quiaia sample respectively. The hot-dust amplitudes of HRQs are systematically lower than Quiaia quasars at a given MIR luminosity and show no clear dependence on the line-of-sight dust extinction,  $E(B - V)$ . We also present the  $6\mu\text{m}$  continuum luminosity as a function of the  $3000\text{\AA}$  continuum luminosity (right) for Quiaia quasars (grey) and HRQs (red). HRQs are systematically off-set to lower MIR luminosities at a given accretion disk luminosity when compared to Quiaia quasars and do not represent a continuation of the Quiaia distributions to higher luminosities. Taken together, this shows that HRQs are poor in both  $2\mu\text{m}$  and  $6\mu\text{m}$  dust relative to Quiaia quasars of similar luminosity.

probes warm dust components with effective temperatures of  $T_{\text{Eff}} \approx 450\text{K}$ . The  $6\mu\text{m}$  luminosities are calculated by conducting a log-linear interpolation between the  $W3$  ( $12\mu\text{m}$ ) and  $W4$  ( $22\mu\text{m}$ ) photometry of each source. HRQs have systematically lower hot-dust amplitudes compared to their blue Quiaia counterparts at any given MIR luminosity. In Fig. 6 (right), we show that HRQs are systematically off-set to lower MIR luminosities than Quiaia quasars of similar optical continuum luminosity, and do not simply represent a continuation of the blue Quiaia distribution to the extreme luminosity regime. Taken together, these results demonstrate that the weaker hot and warm dust emission observed amongst HRQs relative to blue Quiaia quasars is not a luminosity bias (e.g. the ‘receding torus’ Assef et al. 2013, see also the references within) but instead suggests that HRQs represent an evolutionary phase in which the torus-scale dust has been depleted.

Stepney et al. (2026) proposed that the depletion of the torus-scale reservoir observed in HRQs is most likely driven by a blow-out phase (e.g. Hopkins et al. 2005; Hopkins et al. 2008), in which strong radiative feedback ejects or destroys the hottest inner torus component. In this scenario, the remaining dust may be distributed in a much more extended polar rather than equatorial configuration (e.g. Hönig 2019; Stepney et al. 2024). This interpretation is also supported by the lack of correlation between the line-of-sight dust extinction,  $E(B - V)$ , and the hot-dust amplitude in Fig. 6 (left), which suggests that the obscuring medium is not primarily distributed on nuclear scales, but rather, extended to galaxy-wide scales instead.

### 6.3. The origin of the UV excess in luminous, obscured quasars

In this section, we limit our analysis to the 117 HRQs for which it was possible to robustly fit our two-component SED model. In the SPHEREx HRQ sample, we detect a UV excess in 50/66 or equivalently 76 per cent of objects - consistent with the 82 per cent reported in Stepney et al. (2026). The total number of HRQs with blue rest-UV photometric colours is therefore 92/117, or

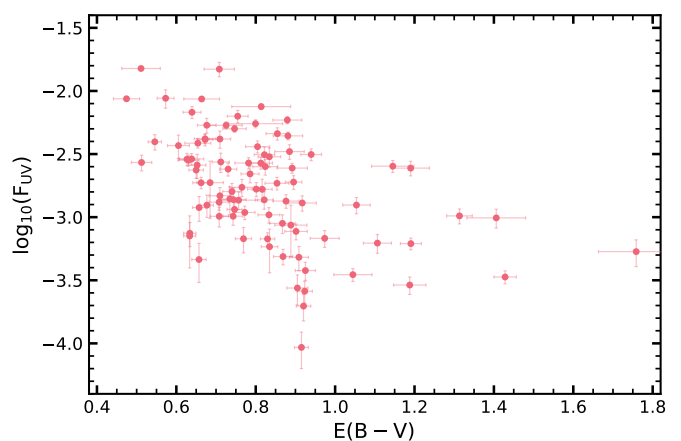


Fig. 7: Logarithm of the scattering fraction as a function of the line-of-sight dust-extinction. We observe an anti-correlation (e.g.  $R_{PCC} = -0.41$  and a  $p$ -value =  $10^{-4}$ ), which suggests that the UV excess suffers modest dust-extinction in HRQs.

equivalently 79 per cent - much higher than reported in the Hot DOG population (e.g. 10-25 per cent; Assef et al. 2016; Li et al. 2024).

The average scattering fraction of HRQs is  $\langle F_{\text{UV}} \rangle_{\text{HRQ}} = 0.26$  per cent, an order of magnitude lower than that observed among blue Hot DOGs (e.g.  $\langle F_{\text{UV}} \rangle_{\text{BHDs}} = 2.62$  per cent; Li et al. 2024). In Stepney et al. (2026), the comparatively modest scattering fractions observed in HRQs were attributed to selection effects driven by the  $(i - K)_{\text{AB}} > 2.5$  colour criterion employed to select the original HRQ sample (e.g. Banerji et al. 2012, 2013, 2015; Temple et al. 2019), which excludes objects with blue rest-UV/optical continua. However, as discussed in Section 2.1, the rest-frame optical to near-infrared colour-selection was not applied when defining the SPHEREx sample, and hence the  $(i - K)_{\text{AB}}$  colour-selection is not responsible for the faint UV excesses observed in the HRQ population.

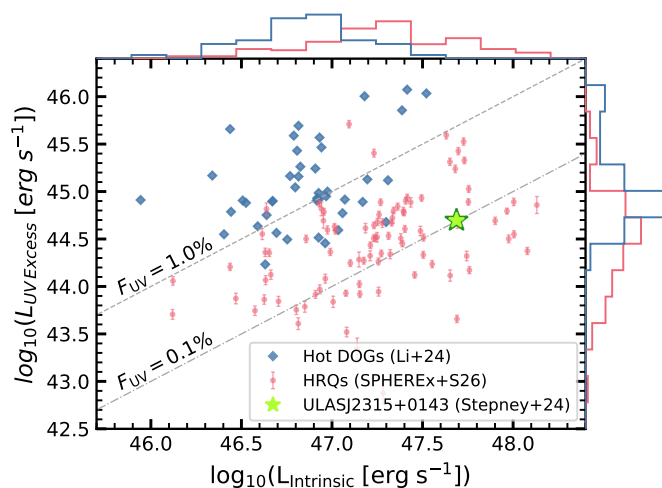


Fig. 8: The dust-corrected 3000Å continuum luminosity of the UV excess vs the intrinsic quasar component. The combined HRQ sample is shown in red and Hot DOGs (e.g. Li et al. 2024) are represented by blue diamonds. Fixed scattering fractions are illustrated by the grey dashed lines. Hot DOGs tend towards higher luminosity scattered components than HRQs. The green star represents the HRQ ULASJ2315+0143, whose VLT-XShooter spectrum has both scattered light and host galaxy signatures in the rest-UV (Stepney et al. 2024).

One interpretation of the weaker scattering fractions observed in HRQs is that the scattered component in the HRQ model may itself suffer from dust-extinction. For example, the Hot DOG SED model has the flexibility to produce scattered components that suffer moderate dust-extinctions (e.g.  $E(B - V)_{\text{Scattered}} = 0 - 0.3$ ; Assef et al. 2015, 2020; Li et al. 2024) which are generally favoured by the SED fitting<sup>11</sup>. The anti-correlation observed between the line-of-sight dust extinction and scattering fraction of HRQs (e.g. Fig. 7;  $R_{PCC} = -0.41$  and a  $p$ -value =  $10^{-4}$ ) is consistent with this behaviour, and hence, the HRQ scattering fractions may be systematically underestimated. However, the lack of HRQs with scattering fractions consistent with the Hot DOG population could also imply that HRQs host intrinsically fainter rest-frame UV excesses, perhaps as a result of differing physical origins for the rest-UV continuum, e.g. star-formation in the host galaxy vs scattered quasar light (Assef et al. 2020; Stepney et al. 2024), differing scattering medium optical depths or different viewing angles.

In Fig. 8, we see that the luminosity of the UV excess is lower in HRQs than in Hot DOGs, despite the intrinsic AGN itself having significantly higher continuum luminosities after correcting for dust. A potential explanation for this result is the post blow-out phase depletion of the hot-dust reservoir observed in HRQs, which may reduce the scattering efficiency of HRQs vs Hot DOGs. In Hot DOGs, the scattering medium has high column densities and is primarily composed of hot, graphite-rich dust (Assef et al. 2022, 2025). Given also their higher X-ray-derived gas column densities compared to HRQs (e.g.  $N_{\text{H}} \sim 10^{23-24} \text{ cm}^{-2}$  vs  $N_{\text{H}} \sim 10^{22} \text{ cm}^{-2}$ ; Assef et al. 2015; Lansbury et al. 2020), Hot DOGs likely represent an earlier stage

<sup>11</sup> Although the additional complexity of the Hot DOG SED model could yield improved fits for some HRQs, many objects lack sufficient optical photometric coverage to constrain such a model. For consistency, we therefore adopt the simpler description of the scattered component for all HRQs.

in the evolutionary sequence in which merger-driven black hole growth is in an earlier phase than in HRQs.

Conversely, in HRQs, enhanced feedback processes powered by super-Eddington accretion may destroy or disperse the hot ( $T_{\text{Eff}} > 1000\text{K}$ ) dust grains which comprise the scattering medium, revealing sight-lines in which star-forming regions in the quasar host can dominate weakly scattered quasar emission. This is particularly true of HRQs with lower luminosity UV excesses with respect to Hot DOGs; such as ULASJ2315+0143 (Fig. 8; green star), spectral analysis of which shows evidence for the rest-UV emission to contain both host galaxy and scattered quasar light signatures. The rest-UV continuum luminosity of ULASJ2315+0143 is consistent with a UV star-formation rate of  $\text{SFR}_{\text{UV}} \approx 100 M_{\odot} \text{ yr}^{-1}$  (Stepney et al. 2024), although ALMA observations suggest that the unobscured SFR of HRQs can exceed  $\approx 1000 M_{\odot} \text{ yr}^{-1}$  (Banerji et al. 2021). In this scenario, HRQs represent a later stage in the evolutionary sequence than Hot DOGs, with HRQs exhibiting a lower luminosity UV excess than ULASJ2315+0143 most likely having host-dominated UV continua.

Crucially, should the scattering mechanism in HRQs and Hot DOGs be the same, with HRQs simply representing a phase where the column density of the scattering medium has been reduced, the polarisation angle of the scattered light in these populations would remain consistent. Therefore, future work should employ image polarimetry techniques (e.g. Assef et al. 2022, 2025) to verify the composition of the scattering medium as well as the polarisation angle of any scattered light in HRQs. Furthermore, spectropolarimetry studies in the most luminous sources will be viable, enabling direct comparisons to other dust obscured quasar populations such as ERQs (e.g. Alexandroff et al. 2018; Zakamska & Alexandroff 2023).

## 7. Conclusions

Using SPHEREx spectrophotometry, we have confirmed a new sample of 76 bright ( $K_{AB} < 18 \text{ mag}$ ) heavily reddened quasars (HRQs) with redshifts  $1.5 \lesssim z_{\text{sys}} \lesssim 3.9$  and line-of-sight dust-extinctions  $0.4 < E(B - V) < 1.6$  ( $A_V \sim 1 - 5 \text{ mag}$ ). To infer the rest-UV to near-infrared spectral energy distribution (SED) properties of the new HRQ sample, we conduct SED fitting on the 76 SPHEREx-confirmed HRQs utilising multi-wavelength surveys spanning the *ugriz - YJHK - W1W2* filters - which correspond to a rest-frame wavelength coverage of  $0.1-3.0 \mu\text{m}$  at  $z_{\text{sys}} \approx 2$ . We show that in most cases a two-component SED model featuring a dust-attenuated quasar component and an additional blue scattered light component provides a good fit to the photometric data - consistent with previous work on HRQs (e.g. Stepney et al. 2026). Our main findings are as follows;

- Using cross-correlation analysis, we show that the spectral resolution of SPHEREx is sufficient to robustly confirm and estimate the redshifts of luminous, dust-obscured, broad-line quasars. We confirm 76 new HRQs with redshifts  $1.5 \lesssim z_{\text{sys}} \lesssim 3.9$  including the first 7 HRQs above  $z = 3$ . Given that SPHEREx is space-based and features a broad wavelength coverage (e.g.  $\lambda \approx 0.75 - 5.0 \mu\text{m}$ ; Doré et al. 2014; Bock et al. 2026), a larger dynamic range in redshift can be probed via SPHEREx than with ground-based facilities such as VLT-SINFONI and Gemini-GNIRS with the highest redshift HRQ at  $z = 3.9$ .
- We find that having accounted for selection effects, the SED properties of the SPHEREx HRQ sample is consistent with HRQ samples studied previously (e.g. Banerji et al. 2012,

2015; Temple et al. 2019; Stepney et al. 2026). Hence, the SPHEREx-confirmed sample represents 76 new bonafide HRQs, increasing the total sample-size to 127 objects spanning redshifts  $1.5 \lesssim z_{\text{sys}} \lesssim 3.9$ .

- Having relaxed the original HRQ mid-infrared colour-selection for the SPHEREx sample to  $(W1 - W2)_{\text{Vega}} > 0.5$  mag, we demonstrate that the new sample is complete in terms of their hot-dust properties. We conclusively demonstrate that HRQs are hot-dust poor with respect to blue Gaia-selected quasars of similar luminosity and redshift -  $\langle L_{\text{Dust}}/L_{\text{Disk}}|_{2\mu\text{m}} \rangle = 1.3 \pm 0.9$  versus  $4.3 \pm 1.3$  for HRQs and blue quasars, respectively and show that this result cannot be explained by a luminosity bias (e.g. the 'receding torus' Assef et al. 2013) Furthermore, we find that the total fraction of HRQs that meet the Jiang et al. (2010) condition for 'hot-dust poorness' is 17 per cent, compared to only 0.3 per cent of blue quasars satisfying the same criteria.
- We detect a rest-UV excess in 50/66 SPHEREx HRQs with photometric data covering the rest-UV. The excess emission can be modelled using a scattered AGN light component, however, contributions to the UV continuum from star-formation in the quasar host galaxy cannot be ruled out. The proportion of HRQs with a UV excess in the SPHEREx sample is consistent with previous work, but significantly higher than observed amongst HRQs (e.g. Assef et al. 2016; Li et al. 2024). The average scattering fraction for all 117 HRQs currently known with sufficient photometric coverage in the rest-UV is  $\langle F_{\text{UV}} \rangle_{\text{HRQs}} = 0.26$  per cent.
- The scattering fractions in HRQs are low compared to Hot DOGs. This can partially be explained by selection effects. The scattered component used to fit Hot DOG SEDs is free to suffer modest dust extinction, whereas, in HRQs the scattered component is completely unobscured. However, despite having lower intrinsic AGN luminosities, the scattered luminosity of Hot DOGs still exceeds that of an average HRQ. This suggests a heterogeneous origin of the UV excess in HRQs, where a lower column-density of obscuring material very close to the black hole potentially results in unobscured sight-lines to star-forming regions in the quasar host galaxy. Thus the host galaxy may dominate the UV excess in some HRQs relative to the scattered light.

Overall, this work demonstrates that SPHEREx spectra are suitable for rapid and efficient confirmation of large numbers of high-redshift, dust-obscured, broad-line quasars enabling their properties to be put in context with other luminous quasar populations. In future work we will expand the samples even further, exploiting the all-sky capabilities of SPHEREx to understand the number densities and multi-wavelength properties of the "hidden monsters" that appear to dominate black hole growth at cosmic noon.

## Data Availability

Table B.1, as well as the photometric data used in this study, are only available in electronic form at the CDS via anonymous ftp to [cdsarc.u-strasbg.fr](ftp://cdsarc.u-strasbg.fr) (130.79.128.5) or via <http://cdsweb.u-strasbg.fr/cgi-bin/qcat?J/A+A/>.

*Acknowledgements.* We gratefully acknowledge funding from ANID CATA BASAL FB210003 (MS, FEB, RJA). MB acknowledges funding from The Royal Society. FEB acknowledges funding from FONDECYT Regular 1241005. RJA acknowledges funding from FONDECYT Regular 1231718. The UHS is a partnership between the UK STFC, The University of Hawaii, The University of

Arizona, Lockheed Martin and NASA. This research uses services or data provided by the Astro Data Lab, which is part of the Community Science and Data Center (CSDC) Program of NSF NOIRLab. NOIRLab is operated by the Association of Universities for Research in Astronomy (AURA), Inc. under a cooperative agreement with the U.S. National Science Foundation. This publication also makes use of data products from the Spectro-Photometer for the History of the Universe, Epoch of Reionization and Ices Explorer (SPHEREx), which is a joint project of the Jet Propulsion Laboratory and the California Institute of Technology, and is funded by the National Aeronautics and Space Administration. Finally, the authors would like to give special thanks to Timothy Y. Brooke and the rest of the IPAC Helpdesk team for their support with this project.

## References

- Ahumada, R., Allende Prieto, C., Almeida, A., et al. 2020, *ApJS*, 249, 3  
Akeson, R., Dubois-Felsmann, G. P., Crill, B. P., et al. 2025, arXiv e-prints, arXiv:2511.15823 (submitted to the ApJ Supplement Series)  
Alexander, D. M., Davis, T. M., Chaussidon, E., et al. 2023, *AJ*, 165, 124  
Alexandrov, R. M., Zakamska, N. L., Barth, A. J., et al. 2018, *MNRAS*, 479, 4936  
Assef, R. J., Bauer, F. E., Blain, A. W., et al. 2022, *ApJ*, 934, 101  
Assef, R. J., Brightman, M., Walton, D. J., et al. 2020, *ApJ*, 897, 112  
Assef, R. J., Eisenhardt, P. R. M., Stern, D., et al. 2015, *ApJ*, 804, 27  
Assef, R. J., Stalevski, M., Armus, L., et al. 2025, *A&A*, 702, A124  
Assef, R. J., Stern, D., Kochanek, C. S., et al. 2013, *ApJ*, 772, 26  
Assef, R. J., Stern, D., Noirot, G., et al. 2018, *ApJS*, 234, 23  
Assef, R. J., Walton, D. J., Brightman, M., et al. 2016, *ApJ*, 819, 111  
Avni, Y. 1976, *ApJ*, 210, 642  
Banerji, M., Alaghand-Zadeh, S., Hewett, P. C., & McMahon, R. G. 2015, *MNRAS*, 447, 3368  
Banerji, M., Jones, G. C., Carniani, S., DeGraf, C., & Wagg, J. 2021, *MNRAS*, 503, 5583  
Banerji, M., McMahon, R. G., Hewett, P. C., et al. 2012, *MNRAS*, 427, 2275  
Banerji, M., McMahon, R. G., Hewett, P. C., Gonzalez-Solares, E., & Koposov, S. E. 2013, *MNRAS*, 429, L55  
Benson, A. J., Bower, R. G., Frenk, C. S., et al. 2003, *ApJ*, 599, 38  
Bluck, A. F. L., Conselice, C. J., Bouwens, R. J., et al. 2009, *MNRAS*, 394, L51  
Bock, J. J., Aboobaker, A. M., Adamo, J., et al. 2026, *ApJ*, 999, 139  
Boersma, C., Maragkoudakis, A., Allamandola, L. J., et al. 2026, *ApJ*, 997, 239  
Calistro Rivera, G., Alexander, D. M., Rosario, D. J., et al. 2021, *A&A*, 649, A102  
Cole, S., Norberg, P., Baugh, C. M., et al. 2001, *MNRAS*, 326, 255  
Costa, T., Rosdahl, J., Sijacki, D., & Haehnelt, M. G. 2018, *MNRAS*, 479, 2079  
Davies, F. B., Bosman, S. E. I., Ganguly, A., et al. 2026, arXiv e-prints, arXiv:2603.10135, (submitted to A&A)  
Di Matteo, T., Springel, V., & Hernquist, L. 2005, *Nature*, 433, 604  
Doré, O., Bock, J., Ashby, M., et al. 2014, arXiv e-prints, arXiv:1412.4872  
Drlica-Wagner, A., Ferguson, P. S., Adamów, M., et al. 2022, *ApJS*, 261, 38  
Dye, S., Lawrence, A., Read, M. A., et al. 2018, *MNRAS*, 473, 5113  
Eisenhardt, P. R. M., Wu, J., Tsai, C.-W., et al. 2012, *ApJ*, 755, 173  
Eisenhauer, F., Abuter, R., Bickert, K., et al. 2003, in *Society of Photo-Optical Instrumentation Engineers (SPIE) Conference Series*, Vol. 4841, Instrument Design and Performance for Optical/Infrared Ground-based Telescopes, ed. M. Iye & A. F. M. Moorwood, 1548–1561  
Elias, J., Joyce, R., Liang, M., et al. 2006, *Proc. SPIE*, 6269  
Euclid Collaboration, Cropper, M. S., Al-Bahlawan, A., et al. 2025a, *A&A*, 697, A2  
Euclid Collaboration, Jahnke, K., Gillard, W., et al. 2025b, *A&A*, 697, A3  
Euclid Collaboration, Mellier, Y., Abdurro'uf, et al. 2025c, *A&A*, 697, A1  
Fawcett, V. A., Alexander, D. M., Brodzeller, A., et al. 2023, *MNRAS*, 525, 5575  
Fawcett, V. A., Alexander, D. M., Rosario, D. J., et al. 2020, *MNRAS*, 494, 4802  
Fawcett, V. A., Harrison, C. M., Alexander, D. M., et al. 2025, *MNRAS*, 537, 2003  
Finnerty, L., Larson, K., Soifer, B. T., et al. 2020, *ApJ*, 905, 16  
Fitzpatrick, M. J., Olsen, K., Economou, F., et al. 2014, in *Observatory Operations: Strategies, Processes, and Systems V*, ed. A. B. Peck, C. R. Benn, & R. L. Seaman, Vol. 9149, International Society for Optics and Photonics (SPIE), 91491T  
Gillette, J., Hamann, F., Lau, M. W., & Perrotta, S. 2024, *MNRAS*, 527, 950  
Goodman, J. & Weare, J. 2010, *Communications in Applied Mathematics and Computational Science*, 5, 65  
Granato, G. L., Zotti, G. D., Silva, L., Bressan, A., & Danese, L. 2004, *ApJ*, 600, 580  
Hamann, F., Zakamska, N. L., Ross, N., et al. 2017, *MNRAS*, 464, 3431  
Hewett, P. C. & Wild, V. 2010, *MNRAS*, 405, 2302  
Hönig, S. F. 2019, *ApJ*, 884, 171  
Hopkins, P. F. & Elvis, M. 2009, *MNRAS*, 401, 7  
Hopkins, P. F., Hernquist, L., Cox, T. J., et al. 2005, *ApJ*, 630, 705

- Hopkins, P. F., Hernquist, L., Cox, T. J., & Kereš, D. 2008, *ApJS*, 175, 356
- Huang, J. S., Glazebrook, K., Cowie, L. L., & Tinney, C. 2003, *ApJ*, 584, 203
- Ishibashi, W., Banerji, M., & Fabian, A. C. 2017, *MNRAS*, 469, 1496
- Ishibashi, W. & Fabian, A. C. 2022, *MNRAS*, 516, 4963
- Jiang, L., Fan, X., Brandt, W. N., et al. 2010, *Nature*, 464, 380
- Jun, H. D., Assef, R. J., Bauer, F. E., et al. 2020, *ApJ*, 888, 110
- Jun, H. D. & Im, M. 2013, *ApJ*, 779, 104
- Juneau, S., Olsen, K., Nikutta, R., Jacques, A., & Bailey, S. 2021, *Computing in Science I& Engineering*, 23, 15
- Kim, Y., Kim, D., Im, M., & Kim, M. 2024, *ApJ*, 972, 171
- Lansbury, G. B., Banerji, M., Fabian, A. C., & Temple, M. J. 2020, *MNRAS*, 495, 2652
- Lawrence, A., Warren, S. J., Almaini, O., et al. 2007, *MNRAS*, 379, 1599
- Li, G., Assef, R. J., Tsai, C.-W., et al. 2024, *ApJ*, 971, 40
- Li, G., Tsai, C.-W., Stern, D., et al. 2023, *ApJ*, 958, 162
- Lisse, C. M., Bach, Y. P., Crill, B. P., et al. 2026, *ApJ*, 1000, L52
- Man, A. W. S., Toft, S., Zirm, A. W., Wuyts, S., & van der Wel, A. 2012, *ApJ*, 744, 85
- McMahon, R. G., Banerji, M., Gonzalez, E., et al. 2013, *The Messenger*, 154, 35
- McMahon, R. G., Banerji, M., Gonzalez, E., et al. 2021, *VizieR Online Data Catalog: The VISTA Hemisphere Survey (VHS) catalog DR5 (McMahon+, 2020)*, *VizieR On-line Data Catalog: II/367*. Originally published in: 2013Msngr.154...35M
- Netzer, H. 2019, *MNRAS*, 488, 5185
- Nikutta, R., Fitzpatrick, M., Scott, A., & Weaver, B. 2020, *Astronomy and Computing*, 33, 100411
- Perrotta, S., Hamann, F., Zakamska, N. L., et al. 2019, *MNRAS*, 488, 4126
- Polletta, M., Tajer, M., Maraschi, L., et al. 2007, *ApJ*, 663, 81
- Rankine, A. L., Hewett, P. C., Banerji, M., & Richards, G. T. 2020, *MNRAS*, 492, 4553
- Richards, G. T., Hall, P. B., Vanden Berk, D. E., et al. 2003, *AJ*, 126, 1131
- Richards, G. T., Strauss, M. A., Fan, X., et al. 2006, *AJ*, 131, 2766
- Rosa, G., Venemans, B., Decarli, R., et al. 2013, *ApJ*, 790
- Sanders, D. B., Soifer, B. T., Elias, J. H., et al. 1988, *ApJ*, 325, 74
- Schaye, J., Crain, R. A., Bower, R. G., et al. 2015, *MNRAS*, 446, 521
- Schneider, D. P., Richards, G. T., Hall, P. B., et al. 2010, *AJ*, 139, 2360
- Somerville, R. S., Hopkins, P. F., Cox, T. J., Robertson, B. E., & Hernquist, L. 2008, *MNRAS*, 391, 481
- Stepney, M., Banerji, M., Hewett, P. C., et al. 2023, *MNRAS*, 524, 5497
- Stepney, M., Banerji, M., Tang, S., et al. 2024, *MNRAS*, 533, 2948
- Stepney, M., Banerji, M., Tang, S., Temple, M. J., & Hewett, P. C. 2026, *Monthly Notices of the Royal Astronomical Society*, 546, stag191
- Storey-Fisher, K., Hogg, D. W., Rix, H.-W., et al. 2024, *ApJ*, 964, 69
- Taylor, M. B. 2005, in *Astronomical Society of the Pacific Conference Series*, Vol. 347, *Astronomical Data Analysis Software and Systems XIV*, ed. P. Shopbell, M. Britton, & R. Ebert, 29
- Temple, M. J., Banerji, M., Hewett, P. C., et al. 2019, *MNRAS*, 487, 2594
- Temple, M. J., Banerji, M., Hewett, P. C., Rankine, A. L., & Richards, G. T. 2021a, *MNRAS*, 501, 3061
- Temple, M. J., Hewett, P. C., & Banerji, M. 2021b, *MNRAS*, 508, 737
- Temple, M. J., Matthews, J. H., Hewett, P. C., et al. 2023, *MNRAS*, 523, 646
- Tsai, C.-W., Eisenhardt, P. R. M., Wu, J., et al. 2015, *ApJ*, 805, 90
- Vanden Berk, D. E., Shen, J., Yip, C.-W., et al. 2006, *AJ*, 131, 84
- Vayner, A., Díaz-Santos, T., Eisenhardt, P. R. M., et al. 2025, *ApJ*, 989, 230
- Weedman, D., Sargsyan, L., Leboutteiller, V., Houck, J., & Barry, D. 2012, *ApJ*, 761, 184
- Wethers, C. F., Banerji, M., Hewett, P. C., et al. 2018, *MNRAS*, 475, 3682
- Wu, J., Tsai, C.-W., Sayers, J., et al. 2012, *ApJ*, 756, 96
- Xia, B., Ramachandra, N., Wells, A. I., Habib, S., & Wise, J. 2025, *arXiv e-prints*, arXiv:2510.07684
- York, D. G., Adelman, J., Anderson, Jr., J. E., et al. 2000, *The Astronomical Journal*, 120, 1579
- Zakamska, N. L. & Alexandroff, R. M. 2023, *MNRAS*, 525, 2716
- Zakamska, N. L., Hamann, F., Pâris, I., et al. 2016, *MNRAS*, 459, 3144

## Appendix A: Confirming heavily reddened quasar candidates with SPHEREx spectrophotometry

In Fig. A.1, we present 12 example SPHEREx spectra spanning a range in redshift, illustrating the effectiveness of our cross-correlation analysis across the full redshift parameter space. In Table A.1, we present the redshift results for all 76 HRQs.

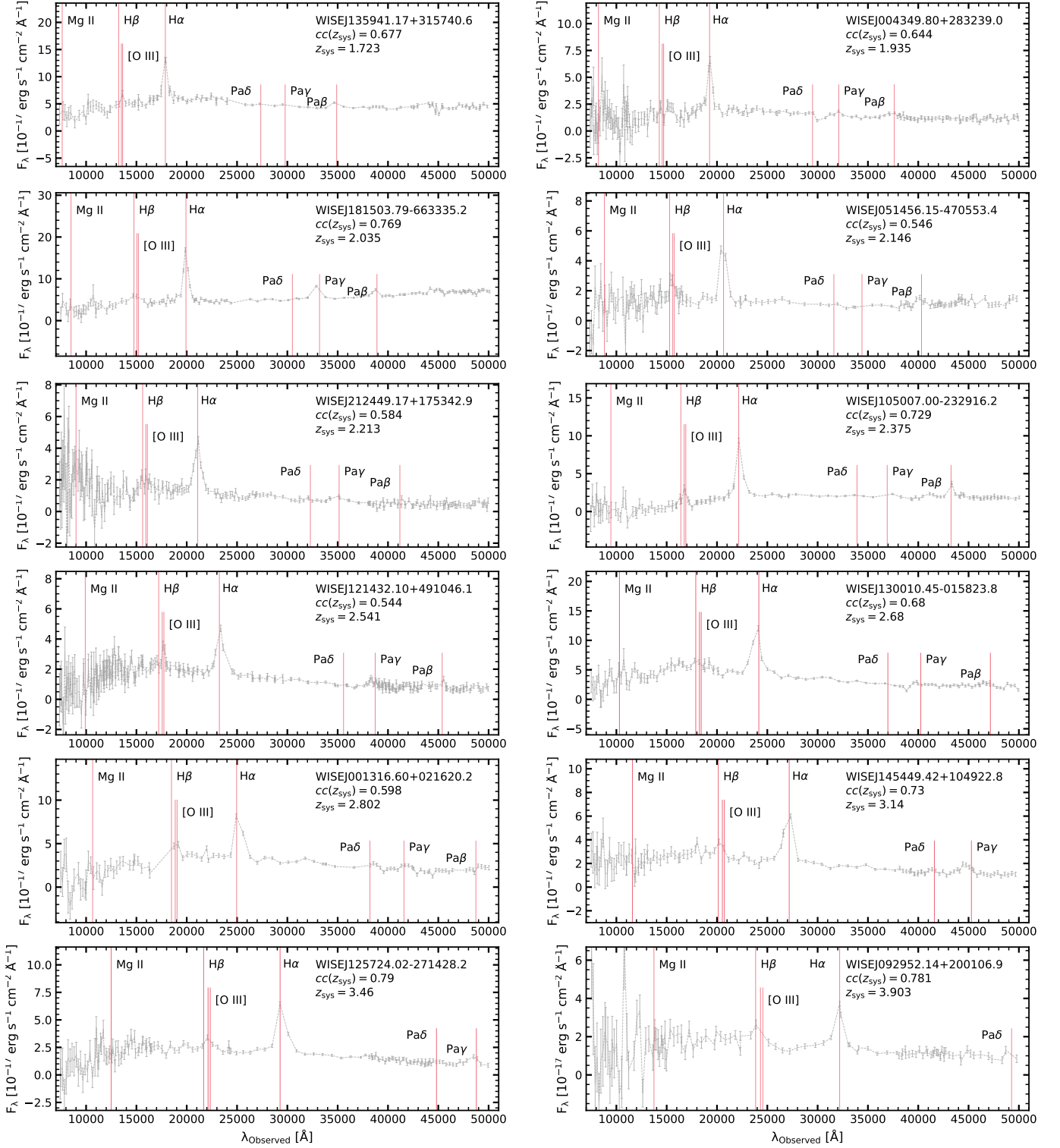


Fig. A.1: We present the SPHEREx spectra for 12 confirmed HRQs which span the full sample range in redshift space. Various emission lines are marked with vertical red lines. The cross-correlation coefficient corresponding to the optimum redshift solution is also presented in each panel.

Table A.1: The co-ordinates,  $K$ -band magnitudes and redshift solutions for our 76 SPHEREx HRQs.

WISE designation	RA [degrees]	Dec. [degrees]	$K_{\text{Vega}}$ [mag]	$z_{\text{sys}}$
WISEJ0009+3608 <sup>a</sup>	2.29665	36.14956	15.85±0.03	2.639±0.003
WISEJ0013+0216	3.31920	2.27230	15.27±0.01	2.809±0.003
WISEJ0020+0814	5.23227	8.24782	15.51±0.02	2.770±0.004
WISEJ0032+1543	8.22131	15.71792	15.13±0.01	2.368±0.003
WISEJ0034-0123	8.52866	-1.39736	15.99±0.02	1.801±0.002
WISEJ0043+2832	10.95753	28.54418	15.81±0.03	1.931±0.004
WISEJ0135+3147	23.81188	31.79294	15.71±0.03	2.380±0.001
WISEJ0146+2121	26.55067	21.36302	16.08±0.04	2.88±0.02
WISEJ0146-3946	26.67365	-39.77846	15.74±0.02	2.210±0.003
WISEJ0152+2608	28.14810	26.13851	15.80±0.03	2.266±0.009
WISEJ0202+1342	30.66227	13.71474	15.10±0.01	2.891±0.003
WISEJ0224-4625	36.23730	-46.42105	15.76±0.02	2.363±0.007
WISEJ0229-4225	37.27422	-42.28606	15.61±0.02	2.413±0.008
WISEJ0236+2637	39.01852	26.62830	15.90±0.03	2.500±0.005
WISEJ0240-0555	40.12126	-5.92019	15.97±0.02	3.43±0.04
WISEJ0311-6309	47.83019	-63.15375	15.22±0.02	2.479±0.003
WISEJ0321+4017	50.25450	40.28816	15.63±0.03	2.26±0.01
WISEJ0326+1547	51.57182	15.79397	15.79±0.03	2.308±0.007
WISEJ0338-1048	54.70936	-10.80746	15.36±0.02	2.165±0.006
WISEJ0347-5643	56.97823	-56.72647	15.64±0.02	2.270±0.003
WISEJ0418-0822	64.67986	-8.36814	15.74±0.02	2.299±0.005
WISEJ0439-3909	69.76437	-39.15342	15.48±0.02	2.240±0.001
WISEJ0442+1040	70.60530	10.66678	15.40±0.02	2.383±0.005
WISEJ0514-4705	78.73398	-47.09819	15.68±0.02	2.145±0.002
WISEJ0612+5629	93.24742	56.48883	15.48±0.02	2.590±0.001
WISEJ0746+4722	115.54396	47.36816	16.06±0.04	2.34±0.01
WISEJ0800+0517	120.16923	5.28665	15.99±0.04	2.351±0.006
WISEJ0819+1901	124.82929	19.01788	15.97±0.04	2.00±0.02
WISEJ0819+3537	124.96216	35.62288	15.48±0.02	1.902±0.004
WISEJ0836+4230	129.22868	42.51441	15.70±0.03	2.460±0.003
WISEJ0929+2001	142.46728	20.0186	16.01±0.04	3.901±0.002
WISEJ1050-2329	162.52919	-23.48785	15.06±0.01	2.374±0.005
WISEJ1056+2535	164.01755	25.59324	15.95±0.03	2.320±0.001
WISEJ1140+0634	175.06440	6.57494	15.80±0.02	2.164±0.006
WISEJ1214+4910	183.63378	49.17948	15.67±0.03	2.540±0.001
WISEJ1252+0715	193.05381	7.25129	14.40±0.01	2.150±0.001
WISEJ1257-2714	194.35010	-27.24119	15.63±0.03	3.460±0.002
WISEJ1300-0158	195.04357	-1.97328	14.72±0.01	2.68±0.01
WISEJ1306-2210	196.69636	-22.16696	15.77±0.03	2.330±0.006
WISEJ1323-1750	200.79116	-17.84267	15.62±0.03	2.375±0.009
WISEJ1325+4921	201.27454	-49.35776	15.82±0.03	2.875±0.005
WISEJ1336+0228	204.12161	2.47703	15.41±0.02	2.282±0.005
WISEJ1341+1005	205.47987	10.09553	15.77±0.02	2.39±0.01
WISEJ1351+4026	207.84937	40.44721	16.08±0.03	2.59±0.01
WISEJ1359+3157	209.92155	31.9613	14.91±0.01	1.720±0.002
WISEJ1424+0315	216.02611	3.25249	15.79±0.02	2.683±0.004
WISEJ1453+1740	223.32730	17.66678	15.39±0.02	2.309±0.002
WISEJ1454+1049	223.70595	10.82300	15.69±0.02	3.14±0.02
WISEJ1455+0324	223.87093	3.40982	15.75±0.02	2.627±0.005
WISEJ1511+0031	227.95365	0.51968	15.59±0.02	2.690±0.001
WISEJ1558+2057	239.56130	20.96097	15.89±0.02	3.000±0.001
WISEJ1648+3447	252.13162	34.79002	16.00±0.03	2.379±0.004
WISEJ1805-6813	271.39146	-68.22513	15.53±0.03	3.570±0.001
WISEJ1806+1909	271.50784	19.15600	15.80±0.03	3.21±0.01
WISEJ1815-6633	273.76583	-66.55979	14.58±0.01	2.040±0.001
WISEJ1815+1612	273.91352	16.20658	15.87±0.03	2.596±0.005
WISEJ1843+4345	280.79209	43.76268	15.15±0.02	2.235±0.009

Table A.1: *Continued*

WISE designation	RA [degrees]	Dec. [degrees]	$K_{\text{Vega}}$ [mag]	$z_{\text{sys}}$
WISEJ1939+4712	294.84363	47.20423	15.68±0.03	2.529±0.004
WISEJ1949+0436	297.38766	4.60399	16.06±0.04	2.073±0.005
WISEJ1952-5629	298.20802	-56.48433	15.32±0.02	2.110±0.007
WISEJ2018+5938	304.57186	59.64462	15.84±0.04	2.291±0.003
WISEJ2020+5931	305.12776	59.52840	15.60±0.03	2.408±0.004
WISEJ2021-7808	305.28283	-78.14237	15.37±0.03	2.274±0.009
WISEJ2059+1225	314.84451	12.42702	15.61±0.02	2.568±0.004
WISEJ2124+1753	321.20488	17.89526	15.91±0.03	2.214±0.009
WISEJ2137-2819	324.37107	-28.31847	15.57±0.02	2.131±0.003
WISEJ2152+2605	328.07529	26.09234	15.83±0.03	2.245±0.005
WISEJ2154+0640	328.56611	6.67735	16.00±0.03	1.929±0.005
WISEJ2213-0534	333.35749	-5.57885	15.90±0.03	2.332±0.008
WISEJ2213+3437	333.44869	34.61899	15.91±0.03	2.516±0.008
WISEJ2222-1746	335.73677	-17.78058	15.67±0.03	2.205±0.005
WISEJ2316+0938	349.19449	9.63618	15.33±0.02	2.19±0.01
WISEJ2320+2919	350.08620	29.32515	16.01±0.03	2.22±0.01
WISEJ2342+4149	355.60148	41.82580	15.64±0.02	2.121±0.003
WISEJ2349+0636	357.47072	6.60591	15.70±0.02	2.235±0.009
WISEJ2359+0640	359.82387	6.68005	15.17±0.01	2.45±0.01

**Notes.** The J2000 coordinates of each HRQ have been truncated to aid readership.

<sup>(a)</sup> This source was also identified in Davies et al. (2026)

## Appendix B: The SED properties of 76 SPHEREx-confirmed heavily reddened quasars

In this appendix, we present the results from our SED analysis discussed in Section 4. We present a complete summary of our results in Table B.1, which will also be made available as online supplementary material at CDS. In addition, Fig. B.1 illustrates SED fits for 12 HRQs with a range in redshift, extinction, hot-dust amplitude and scattering fraction.

Table B.1: The best-fit SED parameters and their corresponding MCMC uncertainties for the 76 SPHEREx HRQs fit with *qSOGEN*.

Object	$z_{\text{sys}}$	$\log_{10}\{\lambda L_{\lambda}(3000\text{\AA})\}$	E(B - V)	F <sub>UV</sub> [%]	$L_{\text{Dust}}/L_{\text{Disk} 2\mu\text{m}}$	$\bar{\chi}_{\nu}^2$	UV Excess
WISEJ0009+3608	2.639±0.003	47.86±0.04	0.97±0.04	–	8.37±0.09	0.6	N/A
WISEJ0013+0216	2.809±0.003	47.96±0.07	0.83±0.03	0.07±0.01	0.89±0.01 <sup>b</sup>	1.3	Conf.
WISEJ0020+0815 <sup>a</sup>	2.770±0.004	47.64±0.07	0.72±0.03	–	0.09±0.02 <sup>b</sup>	1.9	Rej.
WISEJ0032+1543	2.368±0.003	47.47±0.06	0.66±0.02	0.05±0.03	0.96±0.01	0.5	Conf.
WISEJ0034-0123	1.801±0.002	47.50±0.09	1.31±0.07	0.12±0.02	1.02±0.02	1.5	Conf.
WISEJ0043+2832	1.931±0.004	47.63±0.04	1.47±0.05	0.9±0.2	0.38±0.01	21.8	Conf.
WISEJ0135+3147	2.380±0.001	47.27±0.03	0.66±0.07	0.12±0.03	0.69±0.01	4.1	Conf.
WISEJ0146+2121	2.88±0.02	47.49±0.03	0.68±0.02	–	3.76±0.04 <sup>b</sup>	0.6	Rej.
WISEJ0146-3946	2.210±0.003	47.41±0.08	0.88±0.04	0.33±0.06	2.13±0.03	0.3	Conf.
WISEJ0152+2608	2.266±0.009	47.08±0.03	0.63±0.02	0.07±0.02	0.21±0.02	2.9	Conf.
WISEJ0202+1342	2.891±0.003	48.07±0.06	0.90±0.03	0.02±0.01	1.05±0.02 <sup>b</sup>	3.3	Conf.
WISEJ0224-4625	2.363±0.007	47.26±0.04	0.71±0.04	0.42±0.08	2.20±0.04	0.4	Conf.
WISEJ0229-4225	2.413±0.008	47.07±0.06	0.53±0.03	–	0.72±0.02	1.0	Rej.
WISEJ0236+2637	2.500±0.005	47.09±0.03	0.68±0.02	–	0.68±0.07	1.9	Rej.
WISEJ0240-0555	3.43±0.04	47.88±0.07	0.79±0.04	–	0.12±0.02	0.3	Rej.
WISEJ0311-6309	2.479±0.003	47.68±0.09	0.92±0.05	0.01±0.01	0.64±0.01	3.2	Conf.
WISEJ0321+4017	2.26±0.01	47.33±0.03	0.79±0.02	0.02±0.01	0.95±0.01	0.6	Conf.
WISEJ0326+1547 <sup>a</sup>	2.308±0.007	47.46±0.04	1.04±0.04	–	0.06±0.01	1.6	N/A
WISEJ0338-1048	2.165±0.006	47.24±0.01	0.71±0.09	1.49±0.60	1.32±0.03	2.0	Conf.
WISEJ0347-5643	2.270±0.003	47.25±0.04	0.81±0.05	0.26±0.04	2.18±0.04	0.7	Conf.
WISEJ0418-0822	2.299±0.005	47.40±0.08	0.74±0.04	0.17±0.04	1.53±0.03	1.8	Conf.
WISEJ0439-3909	2.240±0.001	47.39±0.03	0.82±0.02	0.25±0.03	0.68±0.02	0.6	Conf.
WISEJ0442+1040	2.383±0.005	47.18±0.04	0.68±0.02	0.12±0.01	1.16±0.01	7.3	Conf.
WISEJ0514-4705	2.145±0.002	47.02±0.02	0.60±0.08	0.38±0.05	4.15±0.06	0.6	Conf.
WISEJ0612+5629	2.590±0.001	47.68±0.03	0.91±0.03	–	3.30±0.04	1.1	N/A
WISEJ0746+4722	2.34±0.01	47.26±0.04	0.94±0.03	0.31±0.03	1.63±0.02	1.0	Conf.
WISEJ0800+0517	2.351±0.006	47.33±0.03	0.86±0.02	–	0.93±0.01	0.5	Rej.
WISEJ0819+1901	2.00±0.02	47.23±0.03	0.90±0.02	0.18±0.02	2.52±0.02	0.5	Conf.

Table B.1: continued.

Object	$z_{\text{sys}}$	$\log_{10}\{\lambda L_{\lambda}(3000\text{\AA})\}$	E(B - V)	$F_{\text{UV}} [\%]$	$L_{\text{Dust}}/L_{\text{Disk}} _{2\mu\text{m}}$	$\bar{\chi}_v^2$	UV Excess
WISEJ0819+3537	1.902±0.004	47.54±0.03	1.05±0.02	–	0.64±0.01	0.7	Rej.
WISEJ0836+4230	2.460±0.003	47.24±0.04	0.70±0.03	–	0.41±0.01	0.5	N/A
WISEJ0929+2001	3.901±0.002	47.73±0.03	0.55±0.02	0.39±0.06	1.85±0.02	1.3	Conf.
WISEJ1050-2329	2.374±0.005	47.90±0.06	1.19±0.08	0.06±0.01	1.13±0.02	4.5	Conf.
WISEJ1056+2535	2.320±0.001	47.03±0.03	0.63±0.02	–	2.22±0.02	2.6	Rej.
WISEJ1140+0634	2.164±0.006	47.26±0.08	0.78±0.04	–	1.02±0.03	0.9	Rej.
WISEJ1214+4910	2.540±0.001	47.40±0.03	0.73±0.02	0.24±0.03	0.84±0.01	1.3	Conf.
WISEJ1252+0715	2.150±0.001	47.74±0.07	0.82±0.04	0.14±0.02	0.66±0.03	1.0	Conf.
WISEJ1257-2714	3.460±0.002	47.99±0.06	0.74±0.02	–	0.63±0.01	1.6	Rej.
WISEJ1300-0158	2.68±0.01	47.81±0.07	0.62±0.04	–	1.85±0.03	1.8	Rej.
WISEJ1306-2210	2.330±0.006	47.31±0.09	0.81±0.05	0.17±0.04	1.98±0.05	1.5	Conf.
WISEJ1323-1750 <sup>a</sup>	2.375±0.009	47.15±0.09	0.64±0.08	0.08±0.02	2.05±0.04	1.7	Conf.
WISEJ1325-4921 <sup>a</sup>	2.875±0.005	48.00±0.04	0.91±0.04	0.11±0.02	0.99±0.02 <sup>b</sup>	0.5	Conf.
WISEJ1336+0228	2.282±0.005	47.23±0.07	0.65±0.04	0.28±0.06	0.99±0.01	1.1	Conf.
WISEJ1341+1005	2.39±0.01	47.41±0.08	0.83±0.05	0.32±0.07	2.68±0.04	3.6	Conf.
WISEJ1351+4026 <sup>a</sup>	2.59±0.01	47.19±0.04	0.66±0.03	–	0.57±0.01	0.7	N/A
WISEJ1359+3157 <sup>a</sup>	1.720±0.002	47.97±0.08	1.42±0.08	0.03±0.01	0.53±0.02	4.8	Conf.
WISEJ1424+0315	2.683±0.004	47.65±0.08	0.85±0.05	0.47±0.09	0.24±0.01	2.0	Conf.
WISEJ1453+1740	2.309±0.002	47.39±0.03	0.75±0.02	0.12±0.02	3.11±0.03	0.4	Conf.
WISEJ1454+1049	3.14±0.02	47.76±0.07	0.67±0.03	0.19±0.03	1.06±0.03 <sup>b</sup>	0.5	Conf.
WISEJ1455+0324	2.627±0.005	47.50±0.08	0.77±0.04	0.07±0.02	0.73±0.03	0.8	Conf.
WISEJ1511+0031	2.690±0.001	47.67±0.09	0.81±0.06	0.37±0.09	1.86±0.04	1.4	Conf.
WISEJ1558+2057	3.000±0.001	47.73±0.04	0.75±0.03	0.63±0.07	0.27±0.01 <sup>b</sup>	2.1	Conf.
WISEJ1648+3447	2.379±0.004	46.96±0.04	0.64±0.03	0.68±0.07	0.95±0.01	1.5	Conf.
WISEJ1805-6813	3.570±0.001	48.17±0.03	0.84±0.03	–	0.08±0.02	0.7	Rej.
WISEJ1806+1909	3.21±0.01	47.70±0.04	0.68±0.02	0.53±0.01	1.20±0.09	1.4	Conf.
WISEJ1815-6633	2.040±0.001	48.01±0.04	1.04±0.08	0.03±0.01	1.98±0.03	4.6	Conf.
WISEJ1815+1612	2.596±0.005	47.48±0.04	0.89±0.03	–	1.08±0.01	1.1	N/A
WISEJ1843+4345	2.235±0.009	47.57±0.04	0.89±0.03	–	0.26±0.01	0.2	N/A
WISEJ1939+4712	2.529±0.004	47.18±0.03	0.65±0.03	–	2.43±0.03	1.9	N/A
WISEJ1949+0436	2.073±0.005	47.46±0.04	1.18±0.04	–	1.64±0.02	0.4	N/A
WISEJ1952-5629	2.110±0.007	47.23±0.04	0.68±0.05	0.20±0.07	0.10±0.01	0.6	Conf.
WISEJ2018+5938	2.291±0.003	47.10±0.03	0.73±0.02	0.14±0.03	2.87±0.03	1.6	Conf.
WISEJ2020+5931	2.408±0.004	47.18±0.04	0.66±0.03	–	2.12±0.02	0.5	N/A
WISEJ2021-7808	2.274±0.009	47.56±0.06	0.93±0.05	0.06±0.02	1.81±0.03	3.1	Conf.
WISEJ2059+1225	2.568±0.004	47.34±0.04	0.63±0.02	0.29±0.03	1.70±0.02	1.5	Conf.
WISEJ2124+1753	2.214±0.009	46.93±0.03	0.57±0.02	0.87±0.09	0.99±0.01	2.6	Conf.
WISEJ2137-2819	2.131±0.003	47.37±0.09	0.83±0.06	0.31±0.08	2.68±0.07	0.4	Conf.
WISEJ2152+2605	2.245±0.005	47.01±0.03	0.67±0.02	0.41±0.04	2.87±0.03	1.8	Conf.
WISEJ2154+0640 <sup>a</sup>	1.929±0.005	47.15±0.03	0.83±0.02	0.06±0.02	1.38±0.01	2.7	Conf.
WISEJ2213-0534	2.332±0.008	47.33±0.04	0.86±0.02	–	1.91±0.03	0.3	Rej.
WISEJ2213+3437	2.516±0.008	47.33±0.04	0.83±0.03	–	0.58±0.01	0.7	N/A
WISEJ2222-1746	2.205±0.005	47.26±0.07	0.82±0.03	–	0.01±0.01	0.5	Rej.
WISEJ2316+0938	2.19±0.01	47.25±0.08	0.70±0.04	0.11±0.02	1.54±0.03	0.8	Conf.
WISEJ2320+2919 <sup>a</sup>	2.22±0.01	46.99±0.04	0.65±0.02	0.24±0.03	1.85±0.02	8.4	Conf.
WISEJ2342+4149	2.121±0.003	47.32±0.03	0.85±0.02	–	1.93±0.02	1.4	Rej.
WISEJ2349+0636	2.235±0.009	47.07±0.05	0.62±0.02	–	1.72±0.05	3.3	Rej.
WISEJ2359+0640 <sup>a</sup>	2.45±0.01	47.48±0.08	0.71±0.04	0.28±0.05	2.42±0.08	1.6	Conf.

**Notes.** The J2000 coordinates of each HRQ have been truncated to aid readership. We quote  $\bar{\chi}_v^2$  statistics from our best two-component SED model where the presence of a UV excess is favoured or from our best single-component model, otherwise. Luminosities are given in units of  $\text{erg s}^{-1}$ .

<sup>(a)</sup> SPHEREx spectra were not used to constrain the rest-frame near-infrared SEDs for these objects.

<sup>(b)</sup> The W2 photometry cannot provide robust constraints on  $L_{\text{Dust}}/L_{\text{Disk}}|_{2\mu\text{m}}$  at these redshifts

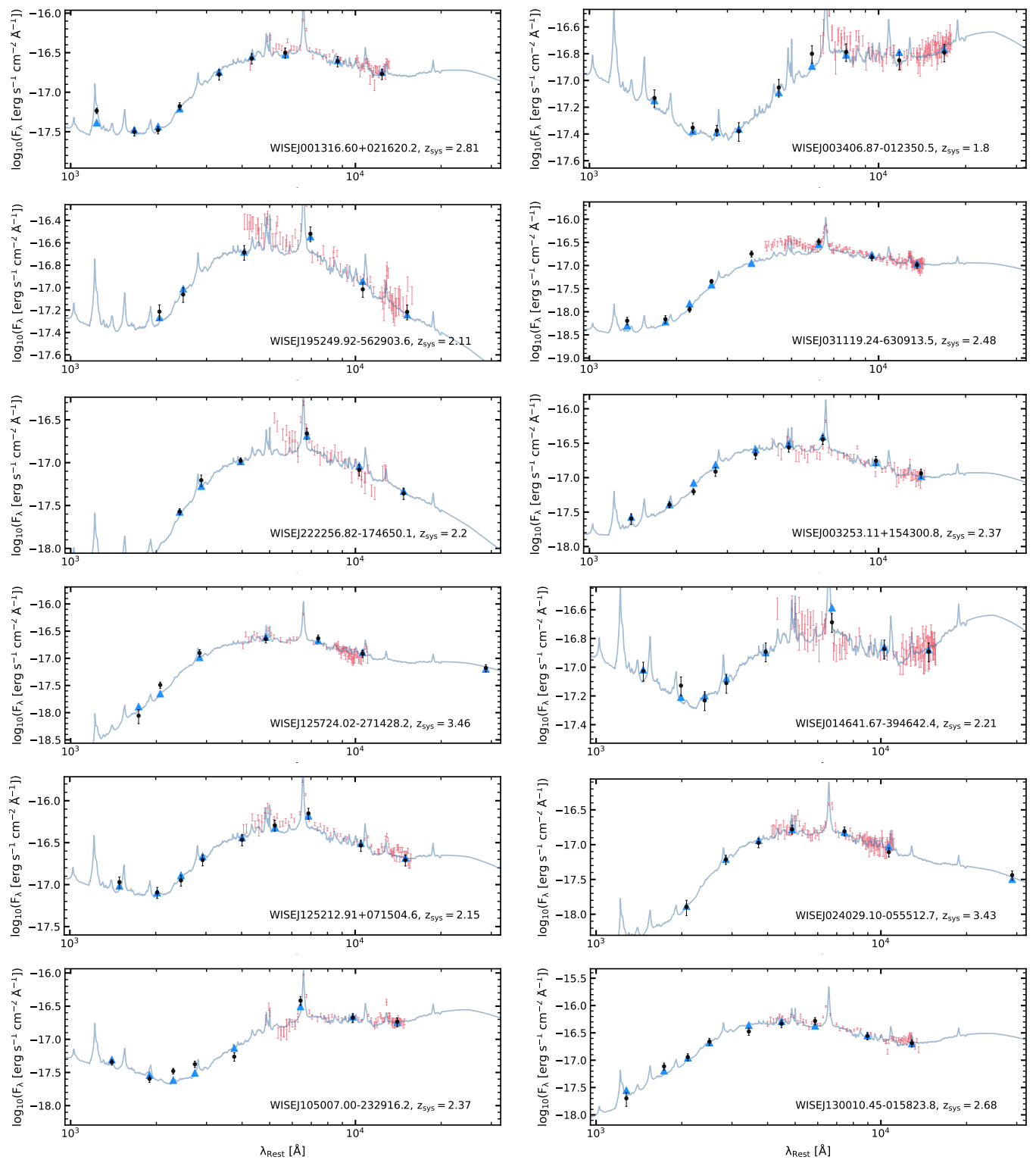


Fig. B.1: We present the "best-fit" QSOGEN SEDs for 12 SPHEREx-confirmed HRQs. The broad-band photometric data from DELVE/SDSS, UKIDSS-LAS/UHS/VHS and WISE are indicated in black with their associated uncertainties. The best-fit multi-component SED models are shown by the blue lines and triangles and the SPHEREx spectra are overlaid in red.

### Appendix C: Hot-dust amplitude completeness in the SPHEREx HRQ sample

To test whether the distribution of hot-dust amplitudes in the SPHEREx HRQ sample is complete, we generate 10000 QSOGEN models whose redshift, line-of-sight dust-extinction and hot-dust amplitude are randomly drawn from uniform distributions with the following limits;  $z_{\text{sys}} = 2.0 - 3.5$ ,  $E(B - V) = 0.4 - 2.0$  and  $L_{\text{Dust}}/L_{\text{Disk}}|_{2\mu\text{m}} = 0.0 - 5.0$ . The  $(W1 - W2)_{\text{Vega}}$  colours are then calculated for each simulated QSOGEN SED. Figure C.1 shows that the SPHEREx selection captures the full diversity of hot dust properties - with all 10000 simulated SEDs meeting the  $(W1 - W2)_{\text{Vega}} > 0.5$  colour-selection. Conversely, the original HRQ sample (e.g. Banerji et al. 2012, 2015; Temple et al. 2019) is only complete at  $L_{\text{Dust}}/L_{\text{Disk}}|_{2\mu\text{m}} > 1$  - consistent with Stepney et al. (2026); their Appendix C. We estimate that the completeness of the original HRQ sample is  $\approx 87$  per cent at  $L_{\text{Dust}}/L_{\text{Disk}}|_{2\mu\text{m}} < 0.5$ .

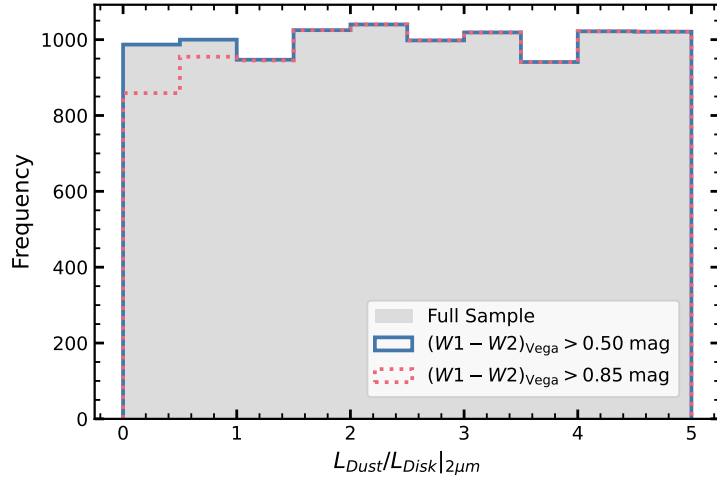


Fig. C.1: Histograms illustrating the distribution of hot-dust amplitudes for 10000 simulated QSOGEN SEDs. The parent sample is presented in grey, the simulated HRQ SEDs which meet the  $(W1 - W2)_{\text{Vega}} > 0.5$  selection used in *this work* are presented in blue, and the simulated SEDs which meet the original HRQ selection (e.g. Banerji et al. 2012, 2015; Temple et al. 2019) are presented in red. The original HRQ selection results in an incomplete sample at  $L_{\text{Dust}}/L_{\text{Disk}}|_{2\mu\text{m}} < 1$  - as suggested by Stepney et al. (2026).